

Clinopyroxene/melt trace-element-partitioning in sodic alkaline magmas

Charles D. Beard^{a,b,*}, Vincent J. van Hinsberg^b, John Stix^b, Max Wilke^{c,d}

^aBritish Geological Survey, The Lyell Centre, Research Avenue South, Edinburgh, EH14 4AP, UK

^bEarth and Planetary Sciences, McGill University, 3450 University Street, Montreal, Québec, H3A 0E8, Canada

^cInstitut für Erd- und Umweltwissenschaften, Universität Potsdam, Golm, Germany

^dChemie und Physik der Geomaterialien, Deutsches GeoForschungsZentrum GFZ, Potsdam, Germany

Abstract

Clinopyroxene is a key fractionating phase in alkaline magmatic systems, but its impact on metal-enrichment processes, and the formation of REE + HFSE mineralisation in particular, are not well understood. To constrain the control of clinopyroxene on REE + HFSE behaviour in sodic (per)alkaline magmas, a series of internally heated pressure vessel experiments was performed to determine clinopyroxene-melt element-partitioning systematics. Synthetic tephriphonolite to phonolite compositions were run H_2O -saturated at 650–825°C with oxygen fugacity buffered to $\log fO_2 \approx \Delta QFM + 1$ or $\log fO_2 \approx \Delta QFM + 5$. Clinopyroxene-glass pairs from basanitic to phonolitic fall deposits from Tenerife, Canary Islands, were also measured to complement our experimentally derived data set.

The REE partition coefficients are 0.3–53, typically 2–6, with minima for high-aegirine clinopyroxene. Diopside-rich clinopyroxene (Ae_{5-25}) prefer the MREE and have high REE partition coefficients (D_{Eu} up to 53, D_{Sm} up to 47). As clinopyroxene become more Na- and less Ca-rich (Ae_{25-50}), REE incorporation becomes less favourable, and both the $V^{I}M1$ and $V^{III}M2$ sites expand (to 0.79 Å and 1.12 Å), increasing D_{LREE}/D_{MREE} . Above Ae_{50} , both M sites shrink slightly and HREE ($V^{I}r_i \leq 0.9$ Å ≈ Y) partition strongly onto the $V^{I}M1$ site, consistent with a reduced charge penalty for $REE \leftrightarrow Fe^{3+}$ substitution.

Our data, complemented with an extensive literature database, constrain a model that predicts trace-element-partition coefficients between clinopyroxene and silicate melt using only mineral major-element compositions, temperature and pressure as input. The model is calibrated for use over a wide compositional range and can be used to interrogate clinopyroxene from a variety of natural systems to determine the trace-element concentrations in their source melts, or to forward model the trace-element evolution of tholeiitic mafic to evolved peralkaline magmatic systems.

Keywords: rare earth elements, aegirine, experimental petrology, Canary Islands, phonolite, peralkaline

1. Introduction

Sodic clinopyroxene appear to more readily incorporate REE than their calcic equivalents (Marks et al., 2004), but despite fractionation of these minerals, melts in evolved alkaline systems can attain high REE contents, even up to economic levels (Kogarko, 1990; Downes et al., 2005; Marks et al., 2011; Sjöqvist et al., 2013; Goodenough et al., 2016; Möller and Williams-Jones, 2016). Trace-element data may be used to model magmatic processes (Spera and Bohrson, 2001; Troll and Schmincke, 2002; Boudreau, 2004; Xu et al., 2010; Girnis et al., 2013; Mungall and Brenan, 2014), but

their interpretation requires precise knowledge of mineral/liquid element-partition coefficients. The approach has been applied to studies of mafic systems and mantle melting processes (Niu, 2004; Workman and Hart, 2005; Foley et al., 2013; Coumans et al., 2016; Peters et al., 2017). However, poor constraints on element-partitioning behaviour in alkaline and peralkaline rocks thus far preclude widespread application in these systems.

Experimental investigations of element-partitioning behaviour in alkali-enriched systems are limited in terms of composition (Wood and Trigila, 2001; Huang et al., 2006), and none yet have explored peralkaline conditions where molar $(Na+K)/Al$ exceeds 1. Additional information has been obtained from nat-

*corresponding author

Email address: cbeard@bgs.ac.uk (Charles D. Beard)

ural samples by measuring the concentration ratios of phenocryst–glass pairs from volcanic and intrusive rocks (Larsen, 1979; Wörner et al., 1983; Shearer and Larsen, 1994; Severs et al., 2009; Fedele et al., 2009; Mollo et al., 2016). However, these results may be biased by the presence of melt inclusions, mineral inclusions and mineral zoning, and their interpretation is commonly complicated by unknown or poorly constrained P-T-H₂O-fO₂ conditions of equilibration and assumptions of closed-system behaviour.

In this contribution, we present trace-element-partition coefficients between sodic clinopyroxene and silicate melts of tephriphonolite to phonolite composition, as determined from internally heated pressure vessel experiments on synthetic and natural compositions. These are complemented by well-constrained natural volcanic phenocryst–glass pairs from Canary Islands pyroclastic fall deposits. We characterise the mineral compositional controls on element-partitioning behaviour and present a predictive model for clinopyroxene/melt element-partitioning that can be used to generate clinopyroxene/melt partition coefficients using only clinopyroxene major-element compositions (e.g., as measured by electron-microprobe). This approach permits forward modelling of element budgets during differentiation processes in magmatic systems, including evolved sodic alkaline systems, as well as providing a mineral-based tool that can be used to reconstruct parental melt compositions from clinopyroxene compositions in natural rocks.

2. Methodology

2.1. Experiment starting materials

Clinopyroxene were synthesised in sodic alkaline silicate melts of varying composition to obtain a range of mineral compositions consistent with those in natural systems. Starting glass compositions are given in Table 1 and Figures S1–S2. Synthetic glasses L1 and L5 were prepared from reagent-grade oxide and carbonate powders, ground together in an agate mortar, de-carbonated for 6 hrs at 450°C, then homogenised in air for 3 hrs at 1400°C in a Pt crucible. Repeated fusion and grinding in agate ensured chemical homogeneity of the starting glasses, which was confirmed by electron-microprobe analyses of the final fused glass. Finely-ground Mud Tank zircon was added to the homogeneous major-element glasses as a source of Zr, Hf, Nb and Ta; the glasses were then fused for a further three hours at 1400°C. The remaining trace-elements were added as a cocktail of single-element nitrate solutions

(ICP-MS standards), dried onto the powdered glasses, then denitrified at 450°C for 30 minutes. The synthetic basanite L1 and phonolite L5 were mixed in varying proportions to make the low alkali (L) series of starting glasses, while dried NaOH and KOH powders were added to make the middle (M) and high (H) alkali starting glasses. Analyses of glass compositions L5 and H5, quenched from superliquidus conditions, confirm that Henry's law was respected (Appendix A).

A well-mixed rock powder from the Nechalacho Layered Suite in Canada (Möller and Williams-Jones, 2016, Unit NLS-9, sample L09-194-405.5, alternative sample name VM 11-6) was used as experimental starting material for a more extreme peralkaline composition. This composition was not fused prior to loading into experiment capsules, so as to preserve the original volatile-element concentrations. An experiment using this material that was quenched from superliquidus conditions is homogeneous with respect to major-elements, as determined from electron-microprobe measurements.

2.2. Experimental equipment and procedures

In total, 36 partitioning experiments were conducted in a Harwood-type internally heated pressure vessel (IHPV) in the HP-GeoMatS laboratory at the German GeoForschungsZentrum (Appendix A). Temperature was measured with Type-S thermocouples calibrated against the melting point of NaCl (Borchert et al., 2010, accuracy of ± 5 °C at 200 MPa). Argon gas was used as the pressure medium, and pressure was measured with a strain gauge to an accuracy of ± 7 MPa. During the experiments, pressure was controlled automatically and held within ± 5 MPa of stated values.

Oxygen fugacity was buffered to the intrinsic redox conditions of the experimental setup, which corresponds to $\log f\text{O}_2 \text{ ca. } \Delta\text{QFM} + 1$ in our H₂O-saturated charges (see Chou, 1986; Berndt et al., 2002; Jugo et al., 2010). One experiment using the Nechalacho Layered Suite composition was performed in a double capsule with a haematite solid buffer, designed to increase $f\text{O}_2$ and promote crystallisation of Fe³⁺-rich clinopyroxene (Eugster and Wones, 1962). This experiment ran at the Hm-Mt buffer, which corresponds to $\log f\text{O}_2 \approx \Delta\text{QFM} + 5$, as confirmed by presence of both buffer minerals in the outer capsule following quench. The experiments were designed to run between the liquidus and solidus for each composition, which corresponds to temperatures between 650 and 825°C, all at 200 MPa pressure (Appendix A).

Powdered starting glass and distilled, deionised water were welded inside 3.0 or 3.5 mm outer diameter platinum capsules of 20–25 mm length (see Appendix A).

To verify that capsules were sealed, they were heated to 110°C and weighed before and after run. The amount of water sealed inside the capsules varied with temperature and composition and was kept in excess of saturation (Carroll and Blank, 1997; Moore et al., 1998; Schmidt and Behrens, 2008). Water saturation was confirmed post-run by puncturing capsules and checking for water expulsion and mass loss on drying at 110°C.

The capsules were loaded into the vessel, pressurised to 200 MPa, then heated to superliquidus temperatures for at least 16 hrs (Appendix A) to permit homogenisation of trace-element concentrations, dissolution of water and equilibration of $f\text{O}_2$ by exchange of H₂ through the capsule wall (cf. Gaillard et al., 2002). Following homogenisation, temperature was lowered to run conditions. An initial set of experiments were cooled rapidly from homogenisation to run temperature at about 100°C/min. A second set of experiments were cooled to run temperature at 1°C/min to promote slow growth of crystals and to minimise the formation of compositional gradients in the melt. Vessel temperature was then cycled between run temperature and run temperature + 10°C to promote dissolution of small crystals at the expense of larger grains, and to promote crystal growth close to the run temperature. Element partitioning results are consistent among experiments of different cooling paths. In all experiments, run temperature was kept constant for at least 40 hrs to allow for chemical homogenisation of melt and growth of crystals via Ostwald ripening. Capsules were then quenched to room temperature.

To minimise the growth of groundmass crystals on cooling, a rapid-quench apparatus was used where possible (Table 2). We have not measured quench rates in this vessel, but the capsules probably cooled at rates of several hundred degrees Celcius per second (e.g. Berndt et al., 2002). For the rest of the experiments, quenching was achieved by cutting power to the furnace, which resulted in cooling to below the glass-transition temperature (< 350°C; Giordano et al., 2005) in less than 150 seconds.

2.3. Natural samples

Alkaline volcanism on Tenerife is associated with a weak thermal mantle plume that impinges upon thick, old, slow-moving oceanic lithosphere (Carracedo et al., 2007). This geological scenario has favoured development of a complex magma-plumbing system that produces a great diversity of volcanic products from alkali basalt to phonolite in composition. The Las Cañadas edifice, a large, central, composite stratovolcano (Bryan et al., 1998; Brown et al., 2003; Edgar

et al., 2007), rests upon a base of at least three mafic alkaline shield volcanoes (Thirlwall et al., 2000; Guillou et al., 2004; Gurenko et al., 2006). Xenoliths indicate that a nepheline syenite intrusive system underlies the island (Wiesmaier et al., 2012).

Six clinopyroxene/glass pairs from four different volcanic eruptions on Tenerife have been investigated. The ~ 2 ka eruptive products of Montaña Blanca and Pico Viejo (Ablay et al., 1995) are phonolitic, plinian fall deposits, whereas Montaña Samara is a monogenetic, mafic cinder cone (Albert et al., 2015). Phase-equilibrium experiments conducted on Montaña Blanca unit UMB-II suggest that magma was stored prior to eruption at 850±15°C, 50±20 MPa, with 2.5±0.5 wt% H₂O at log $f\text{O}_2 \approx \text{NNO} - 0.5$ (Andújar and Scaillet, 2012). Field locations, mineral proportions and major-element compositions of the clinopyroxene and glasses are presented in Appendix A.

2.4. Sample preparation

Experiment capsules were torn open with pliers, and charges were split using a low-speed wafering saw. Samples were mounted in epoxy resin and polished for *in-situ* chemical analyses.

Natural pyroclastic rocks were rinsed in tap water and crushed with a hammer. Crystals and glass fragments, hand-picked from a sieved size-fraction between 1.18 mm and 125 µm, were used to make grain mounts containing 5–20 crystals of clinopyroxene per sample. Natural samples also contain biotite, sanidine, ± spinel, amphibole, olivine, titanite and sodalite. Clinopyroxene mineral mounts were examined using backscattered electron imaging to select euhedral crystals that were free from melt inclusions and chemical zoning (n = 6, Fig. 1).

3. Analytical techniques

All experimental products were examined by reflected-light optical microscopy and scanning electron microscopy, and all phases produced were identified by electron-microprobe using an energy-dispersive detector. Images were obtained to estimate modal proportions of phases, which were calculated using ImageJ freeware (Rasband, 2016, see Appendix A).

3.1. Electron-microprobe analysis

Major-element compositions of experimental products and natural minerals and glasses were measured with a JEOL 8900 instrument at McGill University and a JEOL 8230 instrument at the University of Ottawa

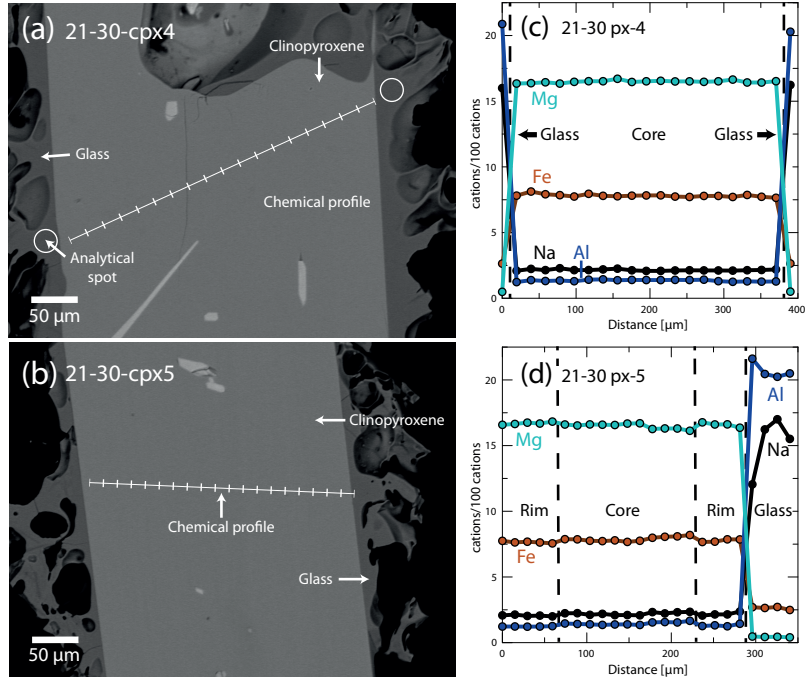


Figure 1: Examples of textural features from Canary Islands clinopyroxene phenocrysts from this study. (a, b) Backscattered electron images show that crystals are euhedral and are free from complex zoning patterns. (c, d) Chemical profiles across clinopyroxene phenocrysts and glass rims (quenched melt), as measured by wavelength dispersive spectroscopy, showing that zoning is effectively absent in these clinopyroxene. In (c) analyses of glass are aligned with the chemical profile shown in (a). Glass analyses shown in (d) are from rims of quenched melt from other clinopyroxene phenocrysts recovered from the same pumice sample. Both pictured phenocrysts are from the basal air fall deposit, associated with the ~2 ka eruption of Pico Viejo, Tenerife (Ablay et al., 1995).

(Table 3). An accelerating voltage of 15 kV was used with a 15 nA beam of 5 μm diameter for minerals, and a 4 nA beam of 50 μm diameter for glasses. Count times for all elements were 60 sec. Using the above routine, we observed no sodium loss over the measurement time period. For the silicate minerals and glasses, both synthetic and natural minerals or oxides were used for calibration (see Appendix A). Analytical uncertainties were determined by multiple analyses of reference materials and duplicate analyses of samples.

Element distribution maps were generated with a JEOL 8900 instrument at McGill University using an accelerating voltage of 15 kV, a focussed 40 nA beam, and a dwell time of 50 ms per pixel (Figs. 3, S3). Fe, Ti, Al, Si and Na were measured with wavelength-dispersive detectors, while Ca and Mg were measured with an energy-dispersive spectrometer.

Transects of Ce, Mg and Fe concentrations within the experiment clinopyroxene were measured with a JEOL 8900 instrument at McGill University using a focussed beam of 50 nA with an accelerating voltage of 20 kV. Ce

was counted with a wavelength-dispersive spectrometer with an LIFH crystal for 100 sec (MAC-Ce standard). Mg and Fe were counted for 20 sec, with TAP and LIF crystals respectively (diopside and olivine standards, respectively). Matrix corrections for Mg, Fe and Ce were not possible with these data, for lack of other major-elements measured, however their relative values may still be used to assess the extent to which the clinopyroxene are chemically zoned.

3.2. Laser-ablation ICP-MS

Trace-element concentrations of clinopyroxene and glasses were determined by laser-ablation ICP mass-spectrometry. Analyses were performed at McGill University using a NewWave 213 nm Nd-YAG laser system coupled to a Thermo Finnigan iCAP-Qc quadrupole ICP-MS instrument. Typical fluence was 3–12 J/cm² (from 80 μm to 8 μm spot sizes), with a repetition rate of 10 Hz. Ablated material was transferred to the ICP-MS in a He flow of 800 mL/min and mixed with Ar prior to injection into the plasma. Instrumental drift was

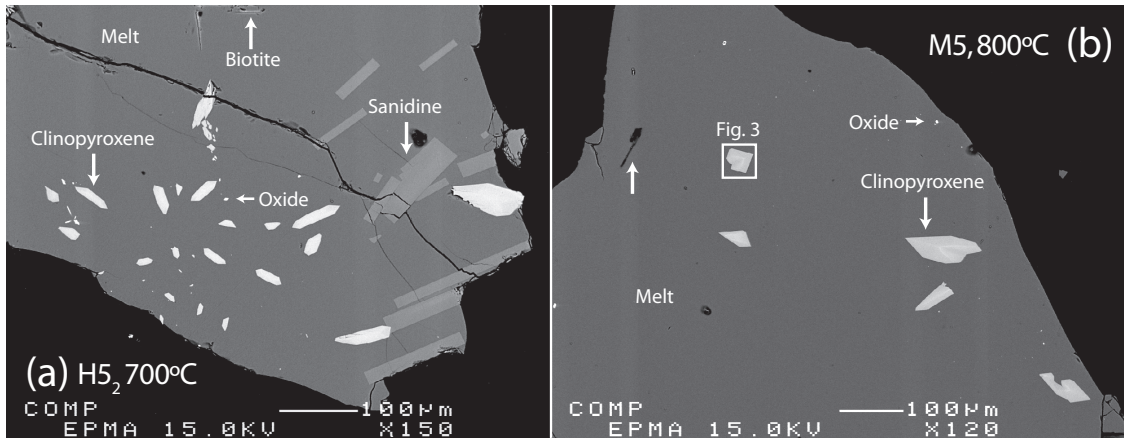


Figure 2: Backscattered electron images showing typical textures of run products from the internally heated pressure vessel experiments. Crystal fractions are typically small (<10% by area), with blade-shaped, euhedral clinopyroxene and glasses free of quench crystals.

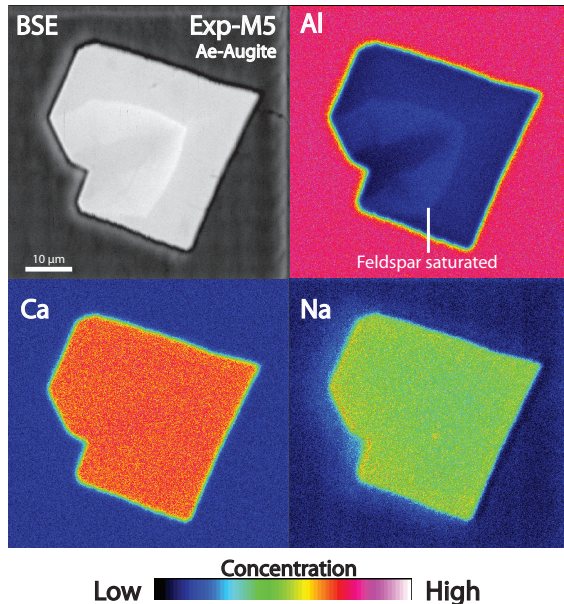


Figure 3: Element maps of clinopyroxene from internally heated pressure vessel experiment M5 (see box in lower magnification image, Fig. 2b). Aegirine-augite clinopyroxene have a sharp internal boundary that reflects feldspar saturation and are subtly zoned. Further element maps are available as an electronic supplement (Fig. S3).

nary Islands clinopyroxene were analysed with beam sizes of 8–80 μm to monitor crater-size-dependent element-fractionation effects; none were found for the elements reported here. For minerals and glasses in the experimental charges, beam sizes of 8–40 μm and 16–80 μm were used, respectively. Depending on grain-size and availability, 5–14 mineral grains and 3–10 areas of glass were analysed per charge. Natural clinopyroxene and rim glasses were analysed using a beam size of 12–80 μm and 12–30 μm , respectively. Wherever possible, ablation was performed along lines parallel to crystal rims (1–3 $\mu\text{m} / \text{sec}$).

Drift corrections and data reduction were conducted with the iolite v2.5 extension for Igor Pro (Paton et al., 2011). The total of major-elements measured by LA-ICP-MS or, where available, the Al concentration from electron-microprobe analyses, was used as an internal standard (Appendix A). For some experiments, ablation through the minerals was too rapid to generate a stable signal for data-reduction purposes. In these cases, a mixing model was applied to estimate the composition of these clinopyroxene, similar to those applied by Rubatto and Hermann (2007); Yang et al. (2018, and see our Appendix C).

monitored by repeat analyses of the primary standard glass BCR-2G, with bias monitored by repeat analyses of secondary standards UTR-2 peralkaline rhyolite and USGS-RGM-1 rhyolite glasses (Appendix A). Sample surfaces were pre-ablated to remove residues from polishing materials and to improve ablation efficiency.

Primary and secondary standards and an unzoned Ca-

4. Results

4.1. Run product phase stability and crystallinity

Trace-element partition-coefficients are reported for eleven experimental charges. 25 additional experiments were rejected as their run temperatures were superliquidus or subsolidus, or because their growth textures

were indicative of disequilibrium (e.g. Fig. S3). Phase proportions are provided in Appendix A.

All reported experimental runs were near-liquidus (3–22% crystals, RL images) and are characterised by a homogeneous distribution of phases (Figs 2, S2), except for experiments H5₃ and NLS-9_{2-HM}, in which sardine crystals are concentrated at the centre. Glasses are clean, homogeneous and show a limited range of major- and trace-element compositions for each experiment (Fig. S1). Clinopyroxene crystals are generally small, euhedral blades with a narrow range of sizes for a given experiment (<10 µm to 100 µm in cross section, Figs. 2–3). In addition to clinopyroxene and glass, experiments on mafic to intermediate compositions produced magnetite, titanite ± kaersutite amphibole, whereas some phonolitic experiments produced biotite, alkali feldspar ± magnetite (Appendix A).

Constraining the full phase equilibria of all of the investigated compositions was beyond the scope of this study. However, in our experiments it can be seen that clinopyroxene has a wide stability field across the investigated physicochemical conditions with only a single starting composition generating amphibole in place of pyroxene (experiments L3 and L3₂). Run conditions and run products given in 2.

4.2. Glass compositions

All run-product glasses are homogeneous across the length and breadth of the experiment capsules based on multiple electron-microprobe and laser-ablation ICP-MS analyses. Most major-element oxide compositions, as measured by electron-microprobe, show relative standard deviations of < 5% within experiment capsules, with minor-elements oxides (concentration < 1%) showing greater variability, most with standard deviations between 5 and 10 % relative. Trace-element compositions of the glass, as measured by laser-ablation ICP-MS, typically show time-weighted relative standard deviations of 1 to 8% within each capsule, with this variability depending on both the absolute concentration of that element and on the beam-size that was used for analyses (Appendix A). Low sum-totals of major-element oxide concentrations in the electron-microprobe analyses are a result of high dissolved-water contents in the quenched melt.

On a total-alkalies vs. silica diagram the experiment glasses are predominantly phonolitic in composition, though span the trachyte-phonolite join (Fig. S1). Their alkalinity index (molar (Na + K)/Al) is 0.85 to 1.40, crossing the alkaline-peralkaline join, and the Mg# of these quenched melts is 0 (Mg-free) to 22. The dissolved water content of these quenched melts is 8.8

to 10.7 wt.% (by difference method from EPMA data, with the Fe oxidation state assigned following Kress and Carmichael 1991) and their NBO/T ratios are 0.98 to 1.42 (Mysen et al., 1982, 1985). The halogen content of the synthetic experiments is nominally zero, whereas glasses from the Nechalacho Layered Suite composition experiments typically contain 0.1 % F and 0.02 % Cl by weight.

The Canary Islands glasses are mostly trachytic to phonolitic, with one basaltic trachy-andesite (sample 17-12, Montaña Samara), and are alkaline to weakly peralkaline in composition (A.I. of 0.78 to 1.16) with Mg# of 8 to 39. Dissolved water content and NBO/T ratios are not reported for these glasses because of post-eruptive loss of volatiles. These Canary Islands glasses typically contain 0.2 % F and 0.4 % Cl by weight.

4.3. Compositions of the clinopyroxene and major-element exchange

Experiments on the synthetic compositions produced clinopyroxene of diopside to aegirine-augite composition (Di₂₉₋₈₂, Ae₉₋₄₅ Hd₇₋₃₃), a subset of which overlap with the compositional space defined by the Canary Islands clinopyroxene on a diopside-hedenbergite-aegirine ternary diagram (Fig. 4a, Table 3 and Appendix A). This low-aegirine group of synthetic clinopyroxene display a positive correlation between ^{IV}Al + ^{IV}Fe³⁺ (in the T-site) and ^{VI}Ti content (in the ^{VI}M1 site, red, *low aegirine*, Ae₅₋₂₅, Fig. 4b), and notably contain both of these elements at elevated concentration relative to the Canary Islands clinopyroxene (^{IV}Al + ^{IV}Fe³⁺ = 0.20–0.49 c.f.u., ^{VI}Ti = 0.07–0.17 c.f.u.). A further subset of synthetic clinopyroxene have higher aegirine content (blue, *med aegirine*, Ae₂₅₋₅₀) and show a similar range of Ti content to the low aegirine synthetic minerals (0.05–0.18 c.f.u.), but a limited range of lower ^{IV}Al + ^{IV}Fe³⁺ content (0.1–0.25 c.f.u., Fig. 4b). Experiments performed on the Nechalacho Layered Suite composition (NLS-9, NLS-9_{2-HM}, green, *high aegirine*, Ae₅₅₋₉₅) reproduced the aegirine-augite to aegirine clinopyroxene from the natural system (Möller and Williams-Jones, 2016) that contain low concentrations of ^{IV}Al + ^{IV}Fe³⁺ (up to 0.14 c.f.u.) and almost no Ti or Mg.

The Canary Islands clinopyroxene that were selected for determination of mineral–melt partition coefficients are diopside in composition (Di₆₅₋₇₁, Ae₃₋₁₀ Hd₂₁₋₂₈), with most crystals containing about 0.05 c.f.u. ^{IV}Al + ^{IV}Fe³⁺ and 0.02 c.f.u. ^{VI}Ti (Fig. 4b). These minerals are free from melt inclusions, suggesting slow rates of crystal growth (Kennedy et al., 1993, Fig. 1). Chemical zonation, if present, is of a similar magnitude to

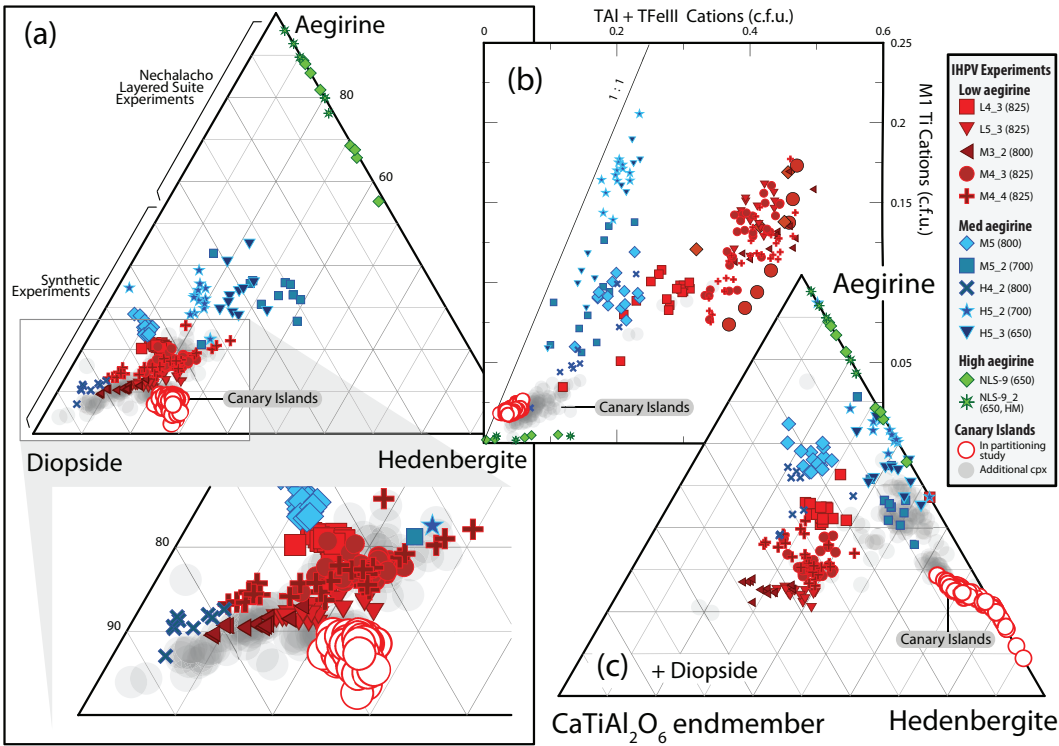
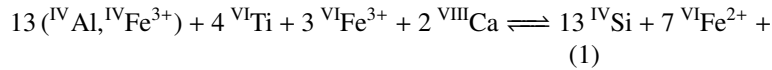


Figure 4: Clinopyroxene grown in internally heated pressure vessel experiments and separated from Canary Islands pyroclasts (a) expressed in terms of diopside, hedenbergite and aegirine end-members, (b) their $V^{I}M^{I}Ti$ and tetrahedral Al and Fe^{3+} contents, and (c) expressed in terms of aegirine, hedenbergite and the theoretical $CaTiAl_2O_6$ end-member (Akasaka and Onuma, 1980). Fe^{2+}/Fe^{3+} within the clinopyroxene was assigned following Droop (1987), then site occupancies and end-member proportions were allocated following Morimoto (1989). For methods used in calculation of the end-member proportions see Appendix F. The range of clinopyroxene compositions within each experiment records changes to the composition of the melt during crystal growth, whereby the cores of the crystals record the first stage of crystallisation and the rims (highest Fe, Na) are in equilibrium with the quenched melt. Rims of these clinopyroxene are preferentially sampled in trace-element analyses by LA-ICP-MS.

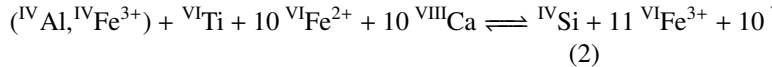
the analytical precision of our electron microprobe, indicating that pressure, temperature and melt composition remained stable during crystal growth (Fig. 1). Trace-element abundances within these Canary Islands clinopyroxene show core-to-rim variations of about 1–5 % relative, with larger variations in element abundance associated with sector zoning than with concentric growth zoning (Appendix A).

By contrast our experiment clinopyroxene display systematic compositional variation between their cores and rims; this variation recording changes to melt composition during growth of these crystals (e.g. Fig. 3). The systematics of crystal-chemical zonation both within individual experimental charges and within groups of experiments reveal major-element exchange vectors between the clinopyroxene and the melt. Three major-element exchange mechanisms correspond to the low (Ae_{5-25}), medium (Ae_{25-50}) and high (Ae_{55-95}) aegirine compositional domains defined above (Figs. 4b,

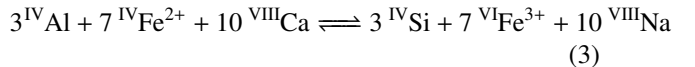
5 and S4).



For the low-aegirine series,



For the medium-aegirine series, and



For the high-aegirine series. As the aegirine content of clinopyroxene increases, substitutions at the ^{IV}T site become relatively less important than exchanges at the

431 $V^{VI}M1$ and $V^{VIII}M2$ sites (Fig. 5). At the $V^{VI}M1$ site, the
 432 importance of Ti substitution for ions of 2+ and 3+ va-
 433 lence also decreases with increasing aegirine content
 434 in the clinopyroxene. In low-aegirine clinopyroxene,
 435 the concentration of 3+ ions at the $V^{VI}M1$ site is neg-
 436 atively correlated with X_{Na}^{M2} , whereas in medium- and
 437 high-aegirine clinopyroxene, the $V^{VI}M1$ site takes pro-
 438 gressively more 3+ ions as X_{Na}^{M2} increases. Substitutions
 439 of $V^{VIII}Ca$ for $V^{VIII}Na$ are relatively unimportant in low-
 440 aegirine clinopyroxene, but play a large role in medium-
 441 and high-aegirine exchange vectors.
 442

**Ends abruptly. add implications for incorporation
mechanisms for trace-elements into clinopyroxene?
Or perhaps just refer to the exchange mechanisms
as in melt section below (Putirka, Mollo)?**

**4.4. Trace-element concentrations in the experiment
clinopyroxene**

448 Assessing the homogeneity of trace-element-
 449 concentrations within minerals is important when
 450 defining mineral–melt partition-coefficients because
 451 only the crystal rims record true chemical equilibrium
 452 with the adjacent melt. In the case of experimental stu-
 453 dies, trace-element analyses of crystal rims are rarely
 454 possible because the mineral grains are commonly
 455 comparable in scale to the beam-size of laser-ablation
 456 or SIMS systems ($\sim 10 - 20 \mu\text{m}$).

457 To quantify the extent to which trace-element-
 458 concentrations are zoned within our experiment
 459 clinopyroxene, we measured electron-microprobe tran-
 460 sects for the elements Mg, Fe and Ce across seven
 461 crystals from three experiments, each crystallised to
 462 varying degrees (Appendix D). These transects re-
 463 veal that clinopyroxene Ce-concentration follows both
 464 sector-zoning and concentric growth-zoning patterns,
 465 as recorded by backscattered electron images and the
 466 XMg of the clinopyroxene. Sector-zoning has a
 467 more pronounced effect on the Ce-concentration in
 468 the clinopyroxene than concentric growth-zoning with
 469 bright sectors on BSE images associated with higher
 470 Ce-concentrations than dark sectors. To gain insight
 471 into the variation of clinopyroxene Ce-concentration
 472 associated with concentric growth-zonation, transects
 473 across grains were averaged *per-experiment*. Ratios of
 474 median average Ce-counts / rim Ce-counts represent the
 475 difference between the composition of the bulk crystal,
 476 as analysed by LA-ICP-MS, and the composition of the
 477 clinopyroxene rims that approach chemical equilibrium
 478 with the adjacent quenched melt. For the three experi-
 479 ments measured, bulk/rim Ce ratios are 1.04 for M3₂,
 480 1.08 for M5 and 1.12 for M3 1.25F (the latter from
 481 Beard, 2018).

482 In the case of compatible elements, the analyses of
 483 bulk crystal trace-element compositions could therefore
 484 return apparent partition coefficients that are overesti-
 485 mated by 4–12% relative to equilibrium values. The
 486 highest values are found for the largest clinopyroxene
 487 crystals and in these, because of their size, we were
 488 able to avoid the cores in the analyses via LA-ICP-MS,
 489 thereby reducing the growth-zonation bias in apparent
 490 trace-element partition-coefficients.

491 Where large clinopyroxene crystals (ca 100 μm) were
 492 present and time-averages of element counts could be
 493 used for the reduction of laser-ablation data, trace-
 494 element-compositions are similar among clinopyroxene
 495 crystals within individual experiments indicating that
 496 trace-element concentrations in the melt phase remained
 497 spatially homogeneous throughout the duration of the
 498 experiments (Appendix A). Typical trace-element con-
 499 centrations in the experiment clinopyroxene are illus-
 500 trated in Figure C.6c in Appendix C.

5. Discussion

5.1. Attainment of equilibrium in the Canary Islands rocks

501 The Canary Islands trace-element partition-
 502 coefficients presented here were determined from
 503 euhedral, blade-shaped crystals free of melt inclusions
 504 and chemical zonation. The corresponding quenched
 505 melt was in direct contact with these crystals and shows
 506 no zonation in backscattered electron images (Fig. 1).
 507 While equilibrium conditions are challenging to con-
 508 firm for a natural volcanic system, the euhedral forms,
 509 chemical homogeneity of crystals, and congruency
 510 between samples from separate eruptions suggest that
 511 the crystals grew in a stable environment, and were not
 512 subject to chemical or physical perturbations during
 513 growth (Fig. 6). In the case of these Canary Islands
 514 clinopyroxene, the entire mineral is interpreted to be in
 515 chemical equilibrium with the adhered quenched melt.

5.2. Chemical heterogeneity and approach toward equilibrium during the experiments

516 During our experiments crystals of clinopyroxene
 517 were grown directly from unseeded glasses and the run
 518 temperature was approached from superliquidus. No at-
 519 tempts were made to reverse these experiments by re-
 520 equilibrating crystals and liquids with deliberately mis-
 521 matched trace-element concentrations because of slug-
 522 gish diffusion of most elements through the clinopyrox-
 523 ene structure (Van Orman et al., 2001; Cherniak and Di-
 524 manov, 2010). As a result of this slow diffusion, all

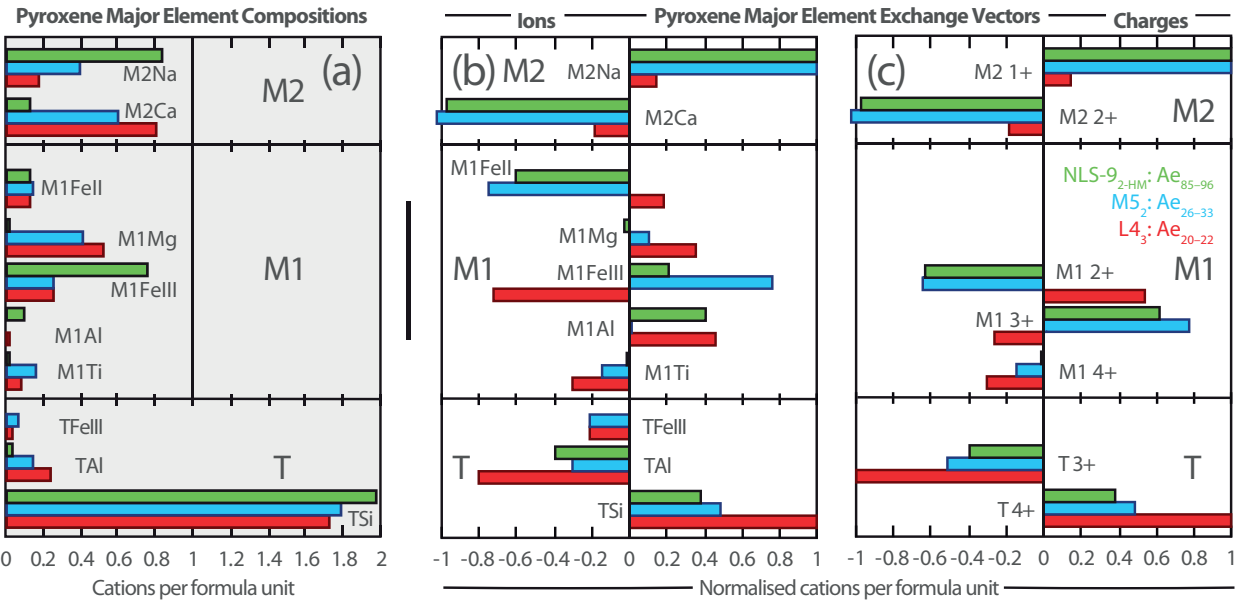


Figure 5: Bar charts showing clinopyroxene composition and major-element exchange mechanisms for three experiments representative of high (green), medium (blue) and low-aegirine (red) clinopyroxene. (a) clinopyroxene major-element compositions are expressed as cations per six-oxygen formula unit (b) exchange mechanisms grouped by ions, (c) grouped by charges. Methods used to calculate these exchange mechanisms are available in the caption of Supplementary Figure S4.

experimental clinopyroxene preserve subtle concentric growth-zonation, generated as the cores of the grains become chemically isolated from the melt during growth (see Fig. 4 and Appendix G). Within our clinopyroxene some sector-zonation is also observed, otherwise the major- and trace-element concentrations are generally uniform in the quenched melt and mineral phases (Appendix A).

We quantify the departure of apparent partition coefficients from equilibrium rim compositions with Ce-transects measured across some experiment clinopyroxene via EPMA, with Ce as a proxy for the other compatible elements (Appendix D). Concentric growth-zoning has a smaller effect on clinopyroxene Ce-concentration than sector zoning, the former of which was isolated by averaging transects across several grains per experiment. Apparent clinopyroxene–melt partition coefficients for compatible elements (median Ce) are offset from equilibrium (rim Ce) to higher values by 4–8% (Appendix D). This systematic positive bias is small relative to the variation in apparent partition coefficients within our sample set, as well as within literature values (e.g. Fig. 7) and shows no correlation with the degree of crystallisation (Appendix D). Furthermore, many of our experimentally-derived apparent partition coefficients plot on trends with clinopyroxene major-

element composition that are defined by a set of literature data (Fig. 7 below). Because the potential bias of our apparent partition coefficients is small relative to the variation in equilibrium values no correction factor has been applied to our data presented in the figures below, or in Table 4 and Appendix A.

5.3. Trace-element-partitioning

Apparent trace-element partition-coefficients and their uncertainties were calculated as mass concentration ratios between clinopyroxene and coexisting glass and are reported in Table 4 and Appendix A. Where trace-element-concentrations in clinopyroxene could be determined using regular time-averages of counts from the ICP-MS system, a time-weighted average composition of clinopyroxene was used with that of the coexisting glass to calculate apparent trace-element partition-coefficients and their associated uncertainty (Appendix A). Where the laser-ablation unmixing model was required for reduction of clinopyroxene trace-element analyses, the partition coefficients were calculated using time-weighted average compositions of glass alongside the corresponding ‘unmixed’ clinopyroxene trace-element concentration (Appendix C). Because a robust-regression data reduction scheme was used, this technique returns a median-average trace-element con-

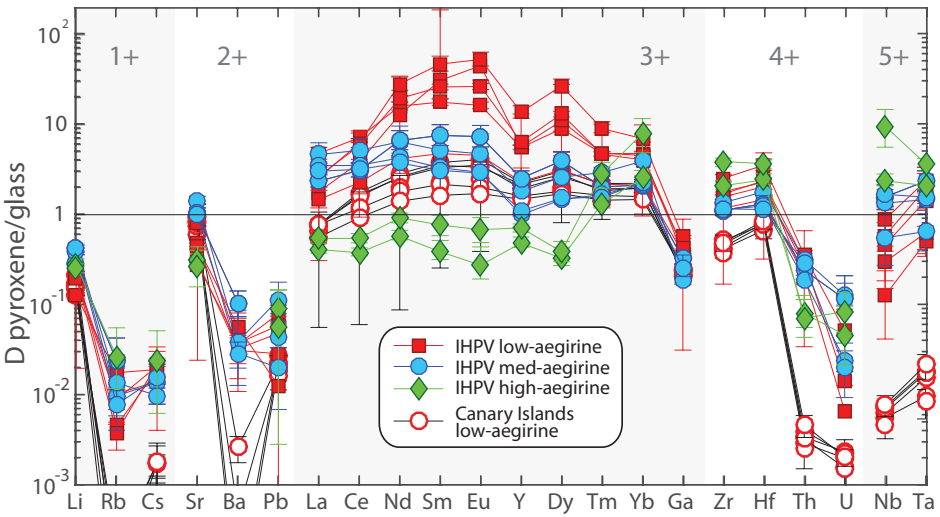


Figure 6: Trace-element partition-coefficients between clinopyroxene and silicate melt, as determined from internally heated pressure vessel experiments ($n = 11$; low-, medium- and high-aegirine types) and from clinopyroxene-rim glass pairs from pyroclastic fall deposits from Tenerife, Canary Islands ($n = 6$; low-aegirine type). Uncertainties on the partition coefficients are at the 1σ level.

centration for clinopyroxene. Derived trace-element partition-coefficients are consistent between these two data-reduction methodologies to better than 2σ . Uncertainty calculations are described in Appendix C.

Three markedly different behaviours of rare earth element partitioning are observed in the experiments (Fig. 6). These depend on the aegirine concentration in the clinopyroxene and match the major-element exchange vector domains discussed above. Low-aegirine experiment clinopyroxene (Ae_{5-25}) prefer the MREE; medium-aegirine clinopyroxene (Ae_{25-50}) show a similar behaviour, save for higher LREE partition coefficients, whereas high-aegirine clinopyroxene (Ae_{55-95}) strongly prefer HREE and show incompatible behaviour for the light and middle REE. The experiment REE partition coefficients are 0.3–53, typically 2–6, with minima for LREE and MREE in high-aegirine clinopyroxene (Fig. 6). Apparent REE partition coefficients determined from our experiments are positively correlated with the ^{IV}Al content of the clinopyroxene and are an order of magnitude higher than most literature values, the majority of which were determined for more mafic compositions (e.g. Fig. 7e). The Canary Islands clinopyroxene show similar rare earth element partitioning systems to the low-aegirine experiment clinopyroxene, with absolute values for these partition coefficients of about one order of magnitude lower (Fig. 6).

The high field-strength elements (HFSE) Zr, Hf, Nb and Ta are compatible to slightly incompatible in the experimental clinopyroxene, and typically 1–2 orders

of magnitude less compatible in the Canary Islands clinopyroxene (Fig. 7a,b,c). D_{HFSE} for the low-aegirine experiments and Canary Islands rocks plot on trends with the ^{IV}Al content of clinopyroxene, as defined by literature data from Italian volcanoes. In our medium- and high-aegirine experiments D_{HFSE} values are not correlated with the ^{IV}Al content of clinopyroxene, consistent with a distinct incorporation mechanism for these elements relative to the low-aegirine experiments. Partition coefficients for the large-ion lithophile elements K, Sr, Pb are positively correlated with X_{Na}^{M2} in the low- and medium-aegirine clinopyroxene, but are lower in high-aegirine clinopyroxene (Fig. 6, Appendix A). The Rb, Cs and Ba partition coefficients have a high uncertainty and are maximum estimates owing to low concentrations of these elements in the clinopyroxene, close to the detection limit for analyses by LA-ICP-MS. Lithium is incompatible ($D_{Li} = 0.1–0.4$) in both Canary Islands and experimental clinopyroxene and, like Sr and Pb, becomes more compatible with increasing aegirine content in the clinopyroxene, plateauing at $X_{Na}^{M2} = 0.4$ and decreasing thereafter (Fig. S5g). The actinides U and Th show contrasting partitioning behaviour; the former showing no correlation with aegirine content in the clinopyroxene, the latter becoming more incompatible with increasing aegirine content (Fig. 7h). The U and Th partition coefficients for our Canary Islands samples are similar to those for the Italian volcanoes (Wood and Trigila, 2001; Fedele et al., 2009; Mollo et al., 2013, 2016), and are 1–2 orders of magnitude more incompat-

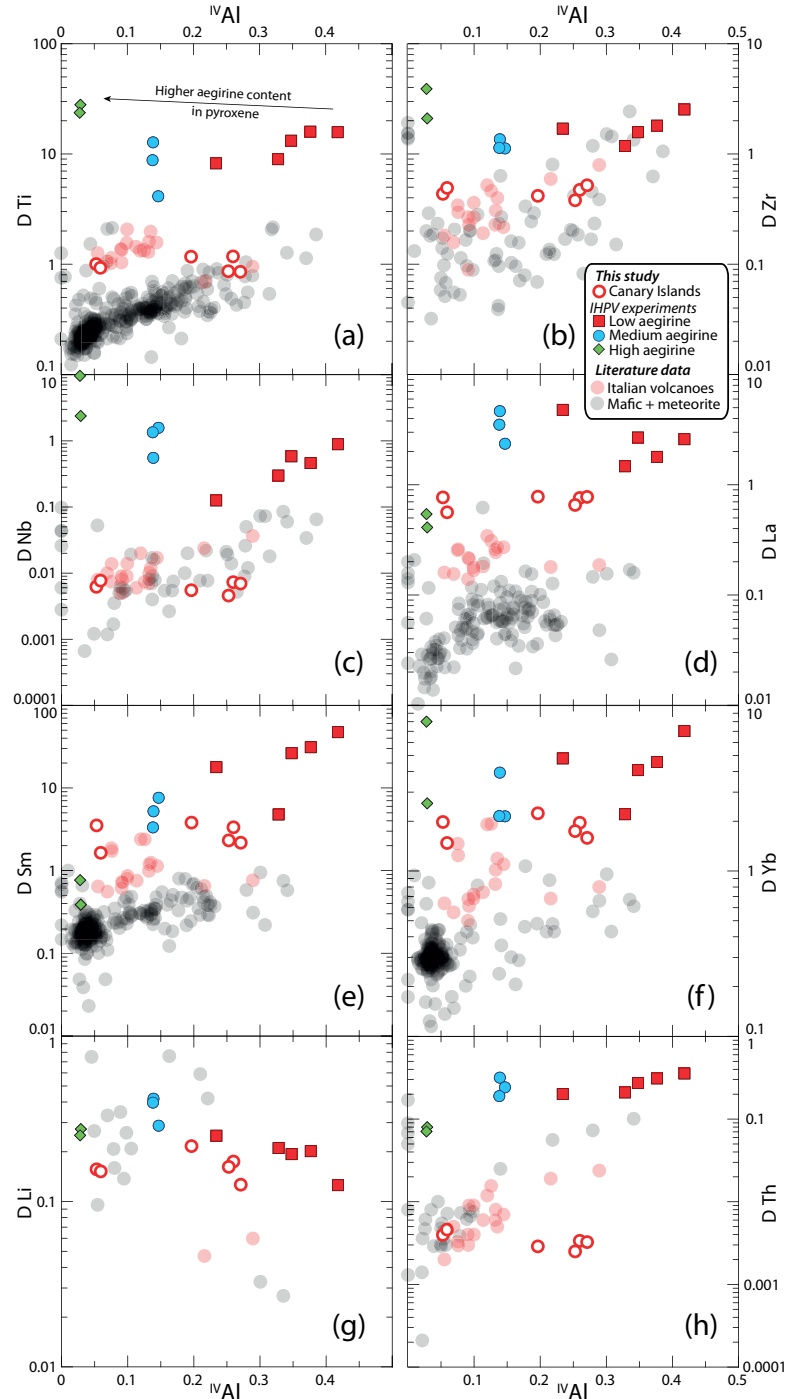


Figure 7: Element partition coefficients for HFSE (Ti, Zr, Nb), REE (La, Sm, Yb) and TE (Li, Th) vs. ^{IV}Al (c.f.u.). Literature values ($n = 411$), including those from potassic Italian volcanoes (red), are from the compilation of Bédard (2014), with additional, more recent, data from Mollo et al. (2016). Figure S5 shows similar diagrams with X_{Na}^{M2} in place of ^{IV}Al .

641 ible relative to the experimental clinopyroxene.

642 5.4. The effects of melt structure on element- 643 partitioning

644 The partitioning of trace-elements between crystals
645 and melts is controlled by their relative activity in each
646 phase and the exchange mechanisms by which their in-
647 corporation into crystals takes place (e.g., Jd-melt, Jd-
648 DiHd and CaTS-DiHd exchanges have been shown to
649 control REE incorporation in cpx, Putirka, 2008; Wood
650 and Blundy, 2014; Mollo et al., 2017). In relatively
651 polymerised systems ($\text{NBO}/\text{T} < 0.49$), melt structure
652 can impart a significant influence on partitioning be-
653 haviour (Gaetani, 2004; Schmidt et al., 2006; Huang
654 et al., 2006). In our strongly depolymerised peralkaline
655 system apparent partition coefficients are not correlated
656 with NBO/T , except for D_{Sr} that shows a weak positive
657 correlation (Fig. 8). NBO/T could not be calculated
658 for our Canary Islands compositions because the water
659 content of the melt prior to quench is not known.

660 5.5. Fits to the lattice-strain model

661 The equilibrium partitioning of trace-elements be-
662 tween minerals and melts is largely controlled by the
663 structure of the crystal lattice, its elasticity (Onuma
664 et al., 1968; Kumazawa, 1969; Weidner and Vaughan,
665 1982) and its ability to accommodate an excess or
666 shortage in charge (Blundy et al., 1998; Wood and
667 Blundy, 2001; Hanchar et al., 2001; Corgne and Wood,
668 2005). The lattice-strain model provides a framework
669 in which the influence of these variables on partition-
670 ing behaviour can be quantified, and thus predicted un-
671 der conditions bracketed by a calibrating data set (On-
672 umra et al., 1968; Blundy and Wood, 1994; Wood and
673 Blundy, 2014). The lattice structure of minerals has
674 a dependence on pressure, temperature and composi-
675 tion, and element-partitioning is a thermodynamically-
676 controlled process (e.g. Wood and Blundy, 1997).

677 Most trivalent ions, including the REE and Y enter
678 the M2 site of clinopyroxene, which is typically 6- or 8-
679 coordinated (Deer et al., 1992). Smaller trivalent ions,
680 including Al, Cr, Ga, Sc, and in the case of Fe-rich
681 clinopyroxene the HREE may enter the smaller ${}^{\text{VI}}\text{M1}$
682 site (Olin and Wolff, 2010; Reguir et al., 2012; Bédard,
683 2014). The high field-strength elements Ti, Zr, Hf, Nb
684 and Ta are typically hosted by the ${}^{\text{VI}}\text{M1}$ site (Hill et al.,
685 2000, 2011; Dugert et al., 2014).

686 To investigate systematics in D_i values and the mech-
687 anisms by which trace-elements are incorporated into
688 clinopyroxene, element-partitioning behaviour was ex-
689 plored in light of the lattice-strain theory, quantitatively
690 described by the lattice-strain equation:

$$691 D_i^{\text{mineral}/\text{melt}} = D_0 \exp \left[\frac{-4\pi E_s N_a}{RT} \left(\frac{r_0}{2} (r_0 - r_i)^2 - \frac{1}{3} (r_0 - r_i)^3 \right) \right] \quad 692$$

693 where r_0 is the ideal radius for the lattice site, E_s is
694 the Young's modulus (i.e., the lattice site stiffness in
695 GPa), D_0 is the strain-free partition coefficient, N_a is
696 Avagadro's number, R is the gas constant, T is temper-
697 ature in Kelvin, and r_i is the ionic radius of the element
698 in question, all radii in Å. We focused on 3+ ions that
699 cover a wide range of radii and fitted lattice-strain pa-
700 rameters for both the ${}^{\text{VI}}\text{M1}$ and ${}^{\text{VIII}}\text{M2}$ sites of clinopy-
701 roxene (Fig. 9):

$$702 D_i^{\text{cpx}/\text{melt}} = D_0^{\text{M2}} \exp \left[\frac{-4\pi E_s^{\text{M2}} N_a}{RT} \left(\frac{r_0^{\text{M2}}}{2} (r_0^{\text{M2}} - r_i)^2 - \frac{1}{3} (r_0^{\text{M2}} - r_i)^3 \right) \right] \\ 703 + D_0^{\text{M1}} \exp \left[\frac{-4\pi E_s^{\text{M1}} N_a}{RT} \left(\frac{r_0^{\text{M1}}}{2} (r_0^{\text{M1}} - r_i)^2 - \frac{1}{3} (r_0^{\text{M1}} - r_i)^3 \right) \right] \quad 704$$

705 Parabolae for 3+ ions were fitted for the ${}^{\text{VI}}\text{M1}$ and
706 ${}^{\text{VIII}}\text{M2}$ sites using the REE, Ga and Al assigned to the
707 ${}^{\text{VI}}\text{M1}$ site of clinopyroxene (Fig. 9a). Fits are weighted
708 based on uncertainties for the element-partition coeffi-
709 cients. HREE have higher element-partition coefficients
710 than can be predicted by substitution into the ${}^{\text{VIII}}\text{M2}$ site,
711 hence were fitted with ionic radii for sixfold coordina-
712 tion into the ${}^{\text{VI}}\text{M1}$ site (cf. Olin and Wolff, 2010; Reguir
713 et al., 2012; Bédard, 2014). Lattice-strain parameters as
714 obtained from fits to the data are shown in Appendix A.

715 In some low-aegirine experiments and the Canary Is-
716 lands rocks, lattice-strain fitting for 3+ ions at the ${}^{\text{VI}}\text{M1}$
717 site was not possible, because too few HREE partitioned
718 onto the ${}^{\text{VI}}\text{M1}$ site of these clinopyroxene. Here, we
719 chose to fit only lattice-strain parameters for the ${}^{\text{VIII}}\text{M2}$
720 site, or fix D_0^{3+} values for the ${}^{\text{VI}}\text{M1}$ site to match those
721 for the ${}^{\text{VIII}}\text{M2}$ site, and fit only the r_0 and E_s pa-
722 rameters for the ${}^{\text{VI}}\text{M1}$ site (Appendix A). Fitting of element-
723 partitioning data for 1+, 2+ and 4+ ions was less suc-
724 cessful owing to sparse coverage of suitable radii and
725 detection-limit issues for some elements. Partition co-
726 efficients for 1+, 2+, and 4+ elements follow radius- and
727 charge-dependent trends consistent with lattice-strain
728 theory and reported effects of charge on lattice-strain
729 parameters (Fig. 9b, e.g., Hazen and Finger, 1979; Law
730 et al., 2000; Adam and Green, 2006).

731 5.5.1. Effects of composition on ideal site size, r_0

732 As the composition of clinopyroxene shifts from
733 augite toward aegirine, the size of the ${}^{\text{VI}}\text{M1}$ and ${}^{\text{VIII}}\text{M2}$

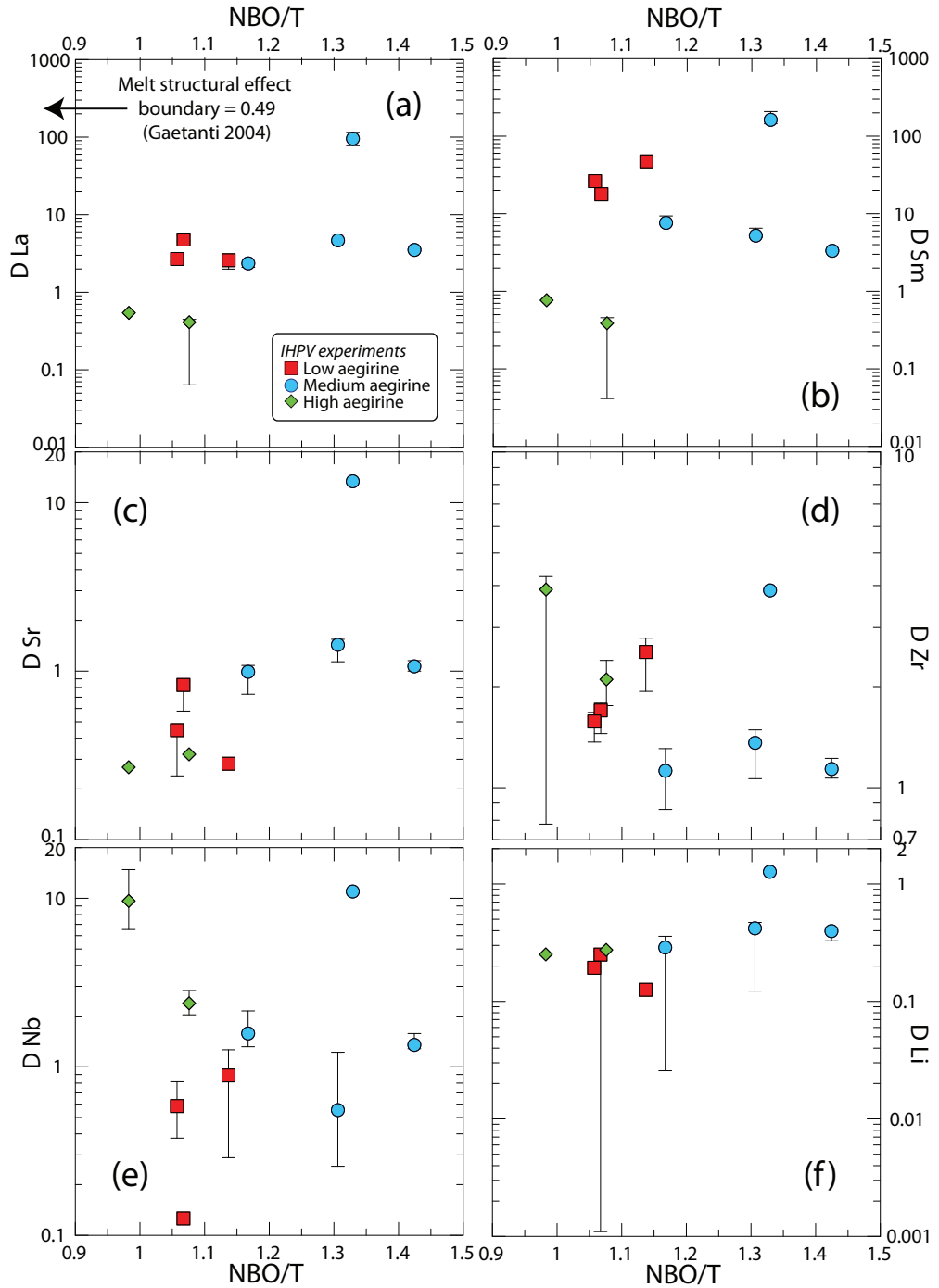


Figure 8: Diagrams of clinopyroxene–melt trace-element partition coefficients for the IHPV experiments as a function of NBO/T of the quenched melt. NBO/T was calculated following Mysen et al. (1985) with melt Fe oxidation state assigned following Kress and Carmichael 1991 and the water content of the melt estimated by difference from 100% major-element oxides.

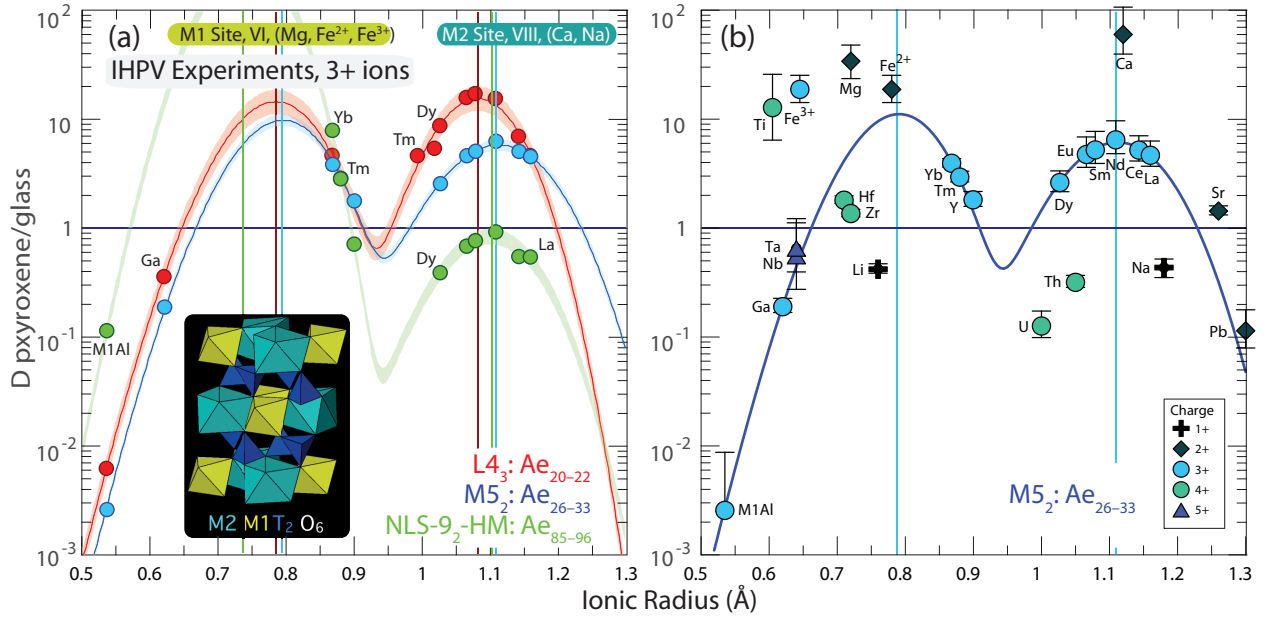


Figure 9: Non-linear weighted least-squares fits to element-partitioning data from the internally heated pressure vessel experiments following the lattice-strain model of Blundy and Wood (1994). (a) Representative fits to 3+ ion partitioning behaviour with examples for low (red), medium (blue) and high-aegirine (green) clinopyroxene experiments. (b) Measured partition coefficients for ions of 1+, 2+, 4+ and 5+ charges that are consistent with the lattice-strain model. Ionic radii are assigned to 6 or 8 fold co-ordination (Shannon, 1976), and were chosen to minimise residuals in the fit (cf. Olin and Wolff, 2010). Y was not included in the fitting routine for 3+ ions because of mass fractionation effects (*ibid.*). Vertical coloured lines indicate ideal ionic radii (r_0) of $^{VI}M1$ and $^{VIII}M2$ sites and shaded areas indicate 95% confidence intervals on the fits determined via bootstrapping. Uncertainties on the partition coefficients in (b) are 1σ . Fitted lattice-strain parameters are given in Table 4.

sites, or strain-free radii (r_0), should diverge following the sizes of the major-element cations on these sites. Lattice-strain fits for 3+ cations indicate expansion of the $^{VIII}M2$ site between low and medium-aegirine clinopyroxene, with r_{0M2}^{3+} correlating well with Na replacing Ca (Figs. 9, 10). Expansion of the $^{VIII}M2$ site stalls at $r_{0M2}^{3+} \approx 1.12 \text{ \AA}$ and $X_{Na}^{M2} \approx 0.4$, changing little in size between medium and high-aegirine clinopyroxene. We suggest that this is a ‘saturation effect’, whereby the smaller ions in the ^{IV}T and $^{VI}M1$ sites prevent further expansion of the $^{VIII}M2$ site as additional R^+ is added to the clinopyroxene. For the $^{VI}M1$ site of clinopyroxene, strain free radii for R^{3+} cations indicate expansion between low and medium-aegirine clinopyroxene and contraction between medium and high-aegirine clinopyroxene (Figs. 9, 10). These trends broadly follow the substitution of Mg^{2+} for Fe^{2+} , then Fe^{2+} for Fe^{3+} with increasing aegirine content in the clinopyroxene.

5.5.2. The effect of cation charge on the D_0 parameter

The D_0 parameter of the lattice-strain model describes ideal, strain-free partitioning and tracks the solubility of an ideal cation in the mineral with chang-

ing pressure, temperature and the bulk composition of the system (Wood and Blundy, 2014). D_0 therefore correlates with the major-element composition of the clinopyroxene. Moreover, incorporation of trace-elements of a different charge introduces an electrostatic penalty that leads to a lower D_0 for that charge (Wood and Blundy, 2001, 2003).

The average charge of major-elements on the $^{VIII}M2$ site of clinopyroxene decreases from 2+ to 1+ on the compositional join between Ca-rich diopside and Na-rich aegirine. Consequently, the electrostatic penalty for substituting a REE^{3+} cation into the clinopyroxene $^{VIII}M2$ site is increased (Fig. 11e). Conversely, as the average charge on the $^{VI}M1$ site of clinopyroxene increases from 2+ toward 3+ in end-member aegirine, the electrostatic penalty incurred when substituting REE^{3+} cations onto the $^{VI}M1$ site is reduced (Fig. 11f). $D_{0,M1}^{3+}$ consequently increases by an order of magnitude between our medium-aegirine and high-aegirine experimental clinopyroxene, an effect that when combined with the shrinking $^{VI}M1$ site size, leads to strong fractionation of the HREE (Figs. 9 and 11f).

A positive correlation between ^{IV}Al and partition co-

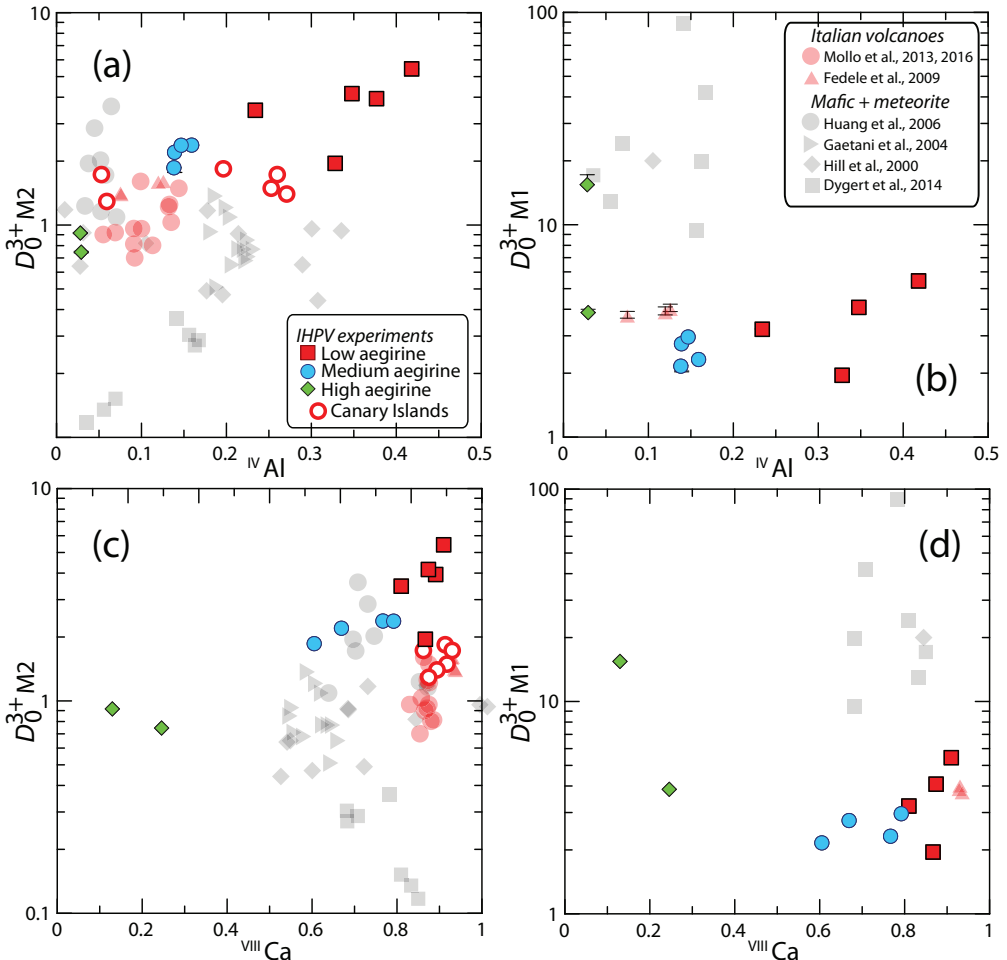


Figure 11: Strain-free partitioning coefficients (D_0) for 3+ ions into clinopyroxene vs. clinopyroxene major-element composition. (a,c) are for the $VIII\text{M}2$ site, and (b,d) are for the $VI\text{M}1$ site. The diagrams show that variability in partitioning behaviour is highly dependent on mineral composition, and that variation between aegirine-rich clinopyroxene cannot be explained well by the same mechanisms as more mafic systems (c). Literature data for element-partitioning in Mafic + Meteorite and Italian volcano compositions are from the compilation of Bédard (2014). 1σ uncertainties are shown in (a, b) and are usually smaller than the symbol sizes.

efficients for highly charged trace-elements has been extensively documented in studies on clinopyroxene (Lundstrom et al., 1994; Gaetani and Grove, 1995; Blundy et al., 1998; Francis and Minarik, 2008; Hill et al., 2011; Mollo et al., 2016). The low-aegirine experimental clinopyroxene and most of the Canary Islands rocks extend trends defined by clinopyroxene from mafic systems (Figs. 7, 11a), whereas the remainder of the experimental data set and Canary Islands rocks show element-partitioning behaviour similar to Italian volcanoes (Wood and Trigila, 2001; Fedele et al., 2009; Mollo et al., 2016), confirming that an $IV\text{Al}$ -controlled substitution mechanism for REE extends to peralkaline conditions (Figs. 7, 11a).

D_0^{3+} parameters for the $VI\text{M}1$ site are strongly correlated with those for the $VIII\text{M}2$ site, except at aegirine concentrations exceeding 50 mol.%. Similarities to $VIII\text{M}2$ partitioning behaviour likely reflect the dominance of T-site substitution mechanisms in augite clinopyroxene. In the high-aegirine clinopyroxene, T-site substitutions become less important as the T-sites become saturated with Si^{4+} (Fig. 5). The replacement of Fe^{3+} at the $VI\text{M}1$ site by 3+ trace-elements does introduce a charge penalty, therefore $D_0^{3+}_{VI\text{M}1}$ increases accordingly.

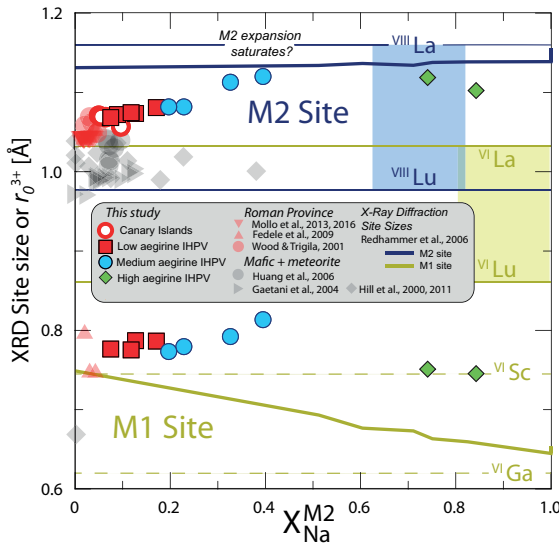


Figure 10: Diagram showing variation of ideal ionic radius r_0^{3+} with $X_{\text{Na}}^{\text{VIII}M2}$ for ${}^{\text{VI}}\text{M1}$ and ${}^{\text{VIII}}\text{M2}$ sites of clinopyroxene. Shown for comparison are single crystal x-ray diffraction data from the hedenbergite-aegirine compositional join (heavy solid lines, from Redhammer et al., 2006). Shaded boxes represent the range of ionic radii for rare earth elements in VI and VIII coordination (Shannon, 1976). Literature data for Italian volcanoes are from Fedele et al. (2009); Mollo et al. (2013, 2016); Wood and Trigila (2001) and for mafic systems are from Hill et al. (2000, 2011); Gaetani (2004); Huang et al. (2006).

799 5.6. An element-partitioning model extending to ae- 800 girine clinopyroxene

801 Partition-coefficients vary systematically with the
802 physicochemical conditions of natural and synthetic
803 magmas (cf. Wood and Blundy, 2003). Consequently, a
804 host of models have been presented to describe the sys-
805 tematics of element-partitioning between clinopyroxene
806 and silicate melts (Wood and Blundy, 1997, 2001; Hill
807 et al., 2011; Yao et al., 2012; Sun and Liang, 2012;
808 Bédard, 2014; Dygert et al., 2014; Mollo et al., 2016).
809 The majority of these models are based on lattice-strain
810 theory and predict how the lattice parameters r_0 , E_s , and
811 D_0 vary with composition, temperature and pressure.
812 This semi-thermodynamic approach theoretically per-
813 mits calculation of partition coefficients for any trace-
814 element, at any set of $P - T - X$ conditions. In reality,
815 all models have a limited working range, as restricted by
816 the input data set. Because existing partitioning models
817 do not reproduce the high $r_{0,M2}^{3+}$ values for clinopyroxene
818 with aegirine contents ≥ 50 mol % (Fig. 12a), they can-
819 not accurately predict REE partitioning behaviour for
820 strongly peralkaline systems. We therefore present a ex-

822 experimental work and natural partition coefficients from
823 Canary Islands rocks ($n = 16$), as well as existing parti-
824 tioning data from the literature ($n = 75$, compilation
825 of Bédard 2014, and Mollo et al. 2016, Fig. 12, Ap-
826 pendix A). Our calibration database covers a wide range
827 of composition, pressure, temperature and oxygen fu-
828 gacity (0.0001–3.5 GPa, 650–1345 °C, $\log f\text{O}_2 = \text{IW}$
829 to $\text{MH} \approx \Delta\text{QFM}$ -5 to +5). Clinopyroxene compo-
830 sitions are $X\text{Mg}$ 0.031–1, X_{Na}^{M2} 0–0.84 and ${}^{\text{IV}}\text{Al}$ 0–0.49
831 c.f.u. and melt composition varies widely in terms of
832 $\text{Mg}\#$ (0–100) and $X\text{H}_2\text{O}$ (0–0.38). REE partition co-
833 efficients are D_{La} 0.01–4.79; D_{Sm} 0.02–47.24, and D_{Yb}
834 0.11–8.00. The majority of partition coefficients in the
835 training data set were measured via SIMS or LA-ICP-
836 MS, minimising analytical uncertainty (e.g. from anal-
837 yses by electron-microprobe).

838 Our model is based on clinopyroxene composition
839 alone so that it may be applied in geological scenarios
840 where melt composition cannot be directly measured,
841 for example to the cores of zoned phenocrysts in tephra,
842 or to cumulate systems. Partition coefficients between
843 clinopyroxene and melt are controlled by the relative
844 activity of elements in each of these two phases (Wood
845 and Blundy, 2014), therefore an empirical model to pre-
846 dict partition coefficients from both melt and mineral
847 compositional terms has the highest potential for accu-
848 racy. Our approach is valid because crystallisation is
849 a thermodynamically-controlled process and the com-
850 position of the melt and thus its effects on element-
851 partitioning are, at least in part, recorded by the major-
852 element composition of the clinopyroxene.

853 5.6.1. The clinopyroxene M2 site

854 To find the principal physicochemical factors that af-
855 fect element-partitioning at the ${}^{\text{VIII}}\text{M2}$ site of clinopy-
856 roxene, a stepwise least-squares multiple linear regres-
857 sion analysis was performed using the lattice-strain pa-
858 rameters r_0^{3+} , E_s^{3+} and D_0^{3+} , temperature, pressure and
859 clinopyroxene composition as inputs. Input parameters
860 were initially examined in binary scatter diagrams to as-
861 certain whether correlations with lattice-strain pa-
862 rameters were linear. If not, interaction compositional terms
863 were added to the initial set of possible fitting pa-
864 rameters that had linear correlations with lattice-strain pa-
865 rameters (e.g. $X_{\text{Al}+\text{Fe}^{3+}}^T$). Intensive variables for mul-
866 tiple regression models for r_0 , E_s and D_0 were intro-
867 duced following a hierarchical forward selection crite-
868 rion with switching. The largest number of significant
869 terms to describe a lattice-strain parameter was eight for
870 E^{M2} (c.95%, cf. Appendix E).

871 The resultant empirical model accounts well for
872 changes in lattice-strain parameters over a range of

compositions from basalt to peralkaline phonolite, faithfully reproducing large r_0^{M2} values typical for sodic clinopyroxene (Fig. 12a, model coefficients in Table 5). Student t-tests show that all of the independent variables included in the models are significant at the 95% confidence level and PRESS R^2 values obtained by repeated random subsampling of the dataset (Stevens, 1996) are close to R^2 values calculated by regular methods, indicating that the models are robust and have high predictive power. Full multiple regression reports are available in Appendix E. Equations generated by the multiple linear regression calculations are given below for the $VIII\text{M}2$ site, where a_i are the regression coefficients for the respective variables:

$$\ln D_0^{M2} = a_1 + a_2 T + a_3 X_{Al+Fe^{3+}}^T + a_4 X_{Ti}^{M1} + a_5 X_{Al-Fe^{3+}}^{M1} + a_6 X_{Fe}^{M2} \quad (6)$$

$$E^{M2} = a_7 + a_8 P + a_9 X_{Al+Fe^{3+}}^T + a_{10} X_{Al}^{M1} + a_{11} X_{Mg}^{M1} + a_{12} X_{Fe}^{M1} + a_{13} X_{Mg}^{M2} + a_{14} X_{Mg}^{M3} \quad (7)$$

$$r_0^{M2} = a_{15} + a_{16} T + a_{17} X_{Al-Fe^{3+}}^{M1} + a_{18} X_{Ti}^{M1} + a_{19} X_{Ca}^{M2} + a_{20} X_{Na}^{M2} \quad (8)$$

The model for r_0^{M2} is robust with high predictive power and incorporates compositional controls from the $\text{VI}\text{M}1$ and $VIII\text{M}2$ sites, as well as temperature. Elevated concentrations of large $VIII\text{M}2$ cations Ca^{2+} and Na^{+} are correlated with large $VIII\text{M}2$ sites. Ti^{4+} cations in the neighbouring $\text{VI}\text{M}1$ site are also correlated with expansion of the $VIII\text{M}2$ site, and the concentration of small Al^{3+} minus larger Fe^{3+} on the $\text{VI}\text{M}1$ site is negatively correlated with r_0^{M2} . The negative correlation between r_0^{M2} and temperature reflects the sum of changes to major-element composition that lead to smaller clinopyroxene $VIII\text{M}2$ sites at higher temperatures. This compositional effect swamps the minor influence of thermal expansion.

The model for D_0^{M2} incorporates compositional terms from all three sites in clinopyroxene and temperature. The positive effect of tetrahedral R^{3+} on D_0^{M2} is the largest contribution to the model, which is consistent with published studies (see above). The relationship between clinopyroxene compositional terms on the $\text{VI}\text{M}1$ and $VIII\text{M}2$ sites and D_0 are indirect and are tied to the solubility of the mineral in the melt (Wood and Blundy,

2003), which in turn is tied to the physicochemical conditions of the system (largely melt composition). The model for D_0^{M2} is less robust than that for r_0^{M2} , largely because there are melt compositional effects that are not recorded in the composition of the clinopyroxene. We tested the Mg# and XH_2O of the melt, neither of which are significant predictors for D_0^{M2} (95% confidence interval).

The model for E^{M2} is less well-constrained than for the other two $VIII\text{M}2$ lattice-strain parameters, suggesting that $VIII\text{M}2$ site stiffness is not tied strongly to clinopyroxene composition, temperature or pressure. Despite a significantly lower predictive power, this model still has physical grounding. Stiffness of the $VIII\text{M}2$ site is positively correlated with pressure, as might be expected following a simple Hooke's law relationship, and there are some subtle compositional controls imparted by the IVT and $\text{VI}\text{M}1$ sites. The poor correlation between E^{M2} , clinopyroxene composition, temperature and pressure is also evident in published element-partitioning models, where E^{M2} is either poorly predicted (Fig. 12b), or set to a fixed value (e.g. Dygert et al., 2014).

Diagrams of measured vs. predicted D values for R^{3+} cations are given in Figure 13a, showing the predictive power of the models over a compositional range between basalt and peralkaline phonolite. For the $VIII\text{M}2$ site, 95% of the measured R^{3+} partition coefficients are reproduced within a factor of $\frac{\pm 2.5}{-2.9}$ (hard dashed lines), and in extreme cases, the model still reproduces D values within an order of magnitude, sufficient for the prediction of element-partitioning trends over a wide range of $P - T - X$. D_{MREE} , such as Sm, are reproduced more faithfully than D_{LREE} , because their radius is closer to r_0^{M2} (Fig. 13c,d), and therefore prediction of their partitioning behaviour is affected less strongly by inaccuracies in predicted E^{M2} values.

5.6.2. The clinopyroxene M1 site

Using a methodology similar to the $VIII\text{M}2$ site, we fitted a predictive model for partitioning of R^{3+} cations onto the smaller $\text{VI}\text{M}1$ site of clinopyroxene. Lattice-strain parabola were constrained by partitioning data for Cr, Ga, Sc, and where suitable, the HREE Tm, Yb and Lu (Our IHPV experiments plus Hill et al. 2000; Fedele et al. 2009; Mollo et al. 2013; Dygert et al. 2014). The training data set for the $\text{VI}\text{M}1$ site partitioning model is small relative to that for the $VIII\text{M}2$ site ($n = 18$), and because it is strongly skewed toward alkaline compositions, it has lower predictive power and is not recommended for application to mafic magmatic systems. Equations for the $\text{VI}\text{M}1$ site lattice-strain parameters, as

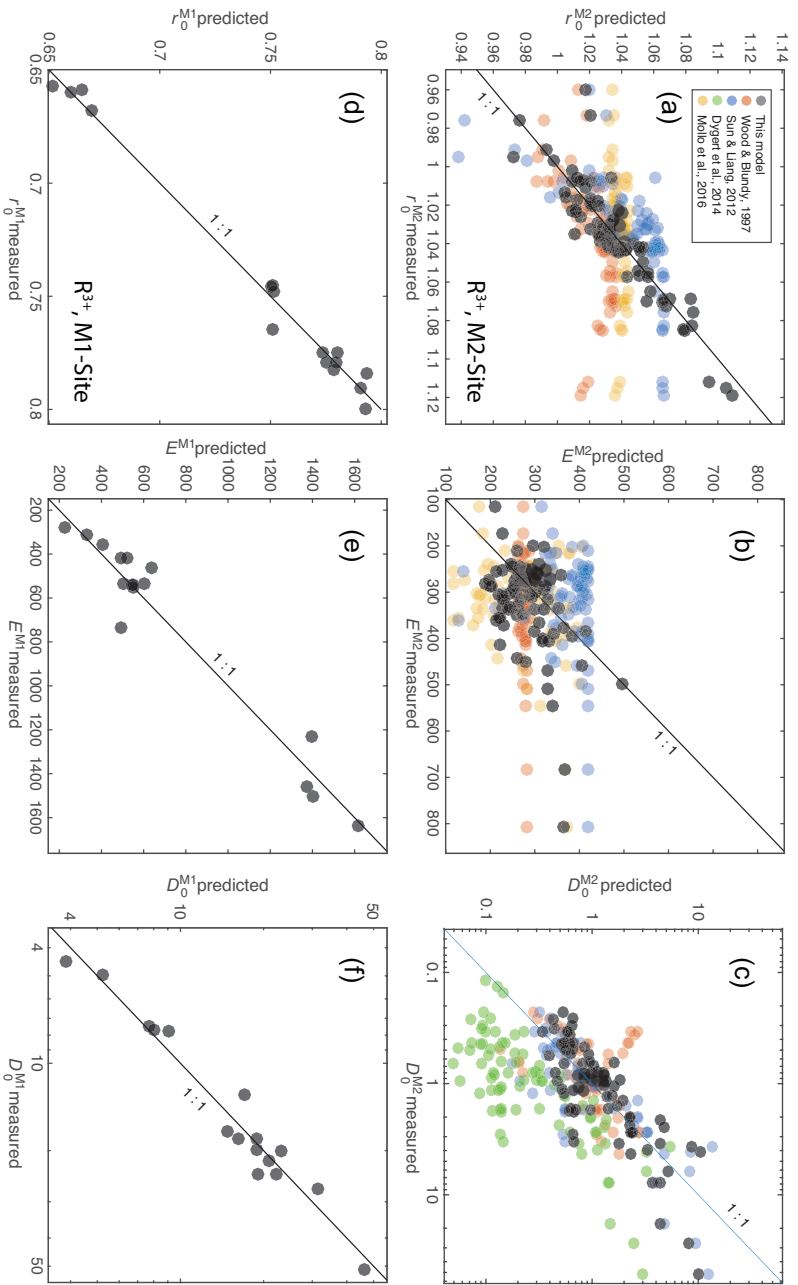


Figure 12: Measured vs. predicted model values for lattice-strain parameters for the $\text{vIII}\text{M2}$ and $\text{vI}\text{M1}$ sites of clinopyroxene. The new models presented here were generated via a stepwise multiple linear regression procedure following a hierarchical forward selection criterion with switching. Full regression reports are in Appendix E and model equations are in the main text.

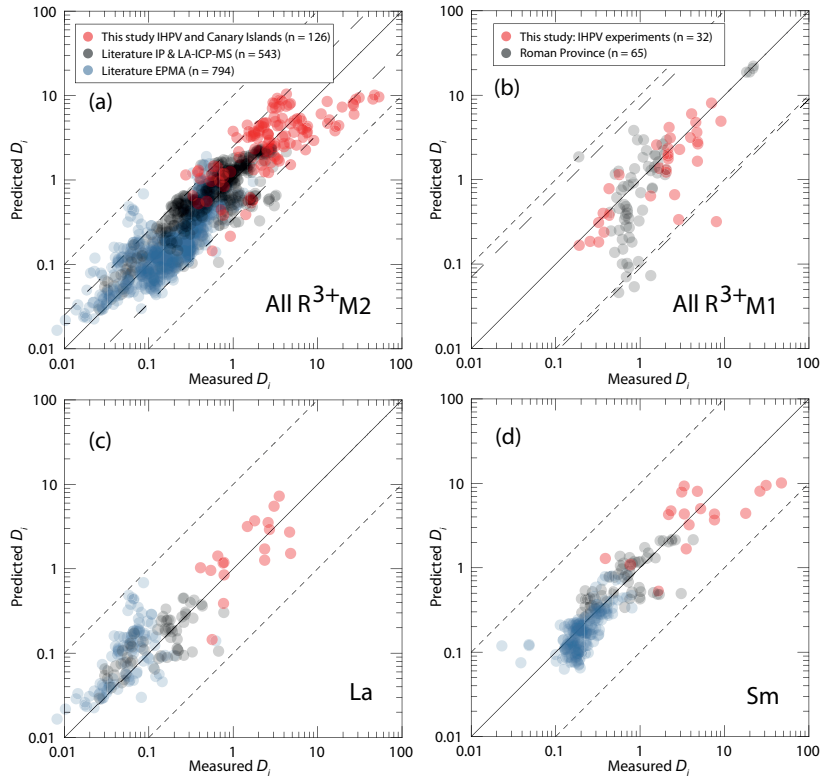


Figure 13: Measured clinopyroxene–silicate melt partition coefficients for 3+ cations vs. those predicted by our empirical model. (a) shows a comparison between measured partition coefficients and model-derived values for the $\text{VIII}^{\text{M}2}$ site of clinopyroxene. Hard dashed lines represent 95% confidence intervals of the model, and correspond to maximum uncertainties of factor $\frac{+2.5}{-2.9}$. Fine dashed lines represent 1 order of magnitude uncertainty (extreme outliers for $\text{VIII}^{\text{M}2}$ model). Partition coefficients in this diagram are the REE La to Er for our IHPV experiments, Canary Islands rocks, and literature data from the Italian volcanoes (Wood and Trigila, 2001; Fedele et al., 2009; Mollo et al., 2013, 2016), and all the REE plus Y for the rest of the data compilation (Bédard, 2014), which is split by analytical methodology. (b) shows performance of the predictive model for the $\text{VI}^{\text{M}1}$ site that is calibrated for alkaline magmatic systems, and includes data from our IHPV experiments and the Italian volcanoes (Fedele et al., 2009; Mollo et al., 2013, 2016). Maximum uncertainties at the 95% confidence interval are a factor of $\frac{+7}{-11}$, higher than for the $\text{VIII}^{\text{M}2}$ site because of the smaller calibrating data set. (c) performance of the $\text{VIII}^{\text{M}2}$ site model for La, and (d) for Sm.

generated by multiple linear least squares regression, are given below and shown in Figure 12 where b_i are the regression coefficients (Table 5) for the respective variables:

$$\ln D_0^{\text{M}1} = b_1 + b_2 X_{\text{Al}}^T + b_3 X_{\text{Fe}^{3+}}^{\text{M}1} + b_4 X_{\text{Ca}}^{\text{M}2} + b_5 X_{\text{Na}}^{\text{M}2} \quad (9)$$

$$E^{\text{M}1} = b_6 + b_7 T + b_8 P + b_9 X_{\text{Mg}}^{\text{M}1} \quad (10)$$

$$r_0^{\text{M}1} = b_{10} + b_{11} P + b_{12} X_{\text{Mg}}^{\text{M}2} + b_{13} X_{\text{Fe}^{3+}}^{\text{M}1} + b_{14} X_{\text{Ca}}^{\text{M}2} \quad (11)$$

The model for $r_0^{\text{M}1}$ is robust and accurately reproduces the input data set. A negative pressure term may

reflect compressional strain on the crystal lattice. Fe^{3+} cations have a positive effect on the size of the $\text{VI}^{\text{M}1}$ site, while smaller Mg^{2+} cations on the neighbouring $\text{VIII}^{\text{M}2}$ site have a negative effect on $\text{VI}^{\text{M}1}$ site size. The small negative $X_{\text{Ca}}^{\text{M}2}$ term is indirectly related to the size of the $\text{VI}^{\text{M}1}$ site.

$E^{\text{M}1}$ is predicted more accurately than $E^{\text{M}2}$ and is largely described by variations in temperature and pressure. Much like the $\text{VIII}^{\text{M}2}$ site, the stiffness of the $\text{VI}^{\text{M}1}$ site appears to be controlled dominantly by physico-chemical factors that are not recorded in the composition of the clinopyroxene.

The model for $D_0^{\text{M}1}$ contains compositional terms from all three crystallographic sites in clinopyroxene. X_{Al}^T has a strong positive correlation with $D_0^{\text{M}1}$, consistent with a charge compensation mechanism that aids

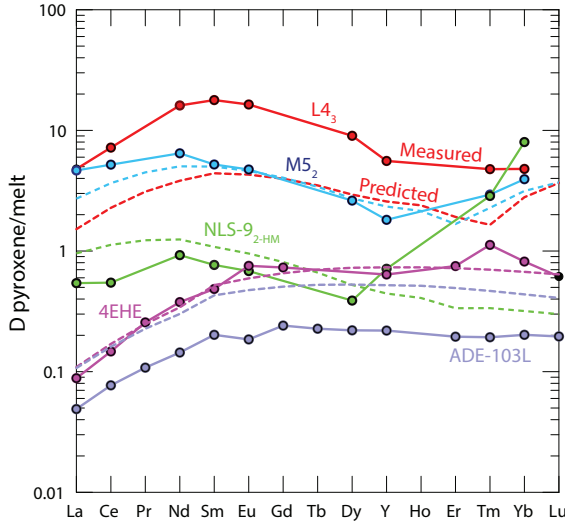


Figure 14: Measured and predicted element-partition coefficients for REE^{3+} . The model does not introduce notable radius-dependent biases, except for in our high-aegirine clinopyroxene (NLS-9_{2-HM} in green) for which D_{HREE} are strongly underpredicted, owing to inaccurate return of $D_0^{\text{M}1}$. Shown for comparison are two diopside–melt pairs: 4EHE from Hill et al. (2000), grown from a synthetic (NC-MAS) basaltic andesite composition and ADE-103L from Lofgren et al. (2006) grown from a picritic composition based on the Angra dos Reis meteorite.

incorporation of R^{3+} cations, while terms for $\text{VI}_{\text{M}1}$ and $\text{VIII}_{\text{M}2}$ site cations may be indirectly recording melt compositional effects. Because $D_0^{\text{M}1}$ is unusually high for our high-aegirine experiments, they had to be excluded from the fitting procedure to permit model convergence. Therefore while the models for $r_0^{\text{M}1}$ and $E^{\text{M}1}$ are calibrated for use all the way to end-member aegirine the model for the $D_0^{\text{M}1}$ term is only calibrated for use up to $\sim \text{Ae}_{50}$. Further experiments at conditions between those that generated our medium and high-aegirine clinopyroxene would be required to better constrain the clinopyroxene compositional record of $D_0^{\text{M}1}$ in strongly peralkaline Fe-rich magmas.

When applied to our experimental data, and the compilation of partition coefficients from Italian volcanoes (Fedele et al., 2009; Mollo et al., 2013, 2016), the $\text{VI}_{\text{M}1}$ stepwise model reproduces element-partitioning data to a factor of $\frac{+7}{-11}$ at the 95% confidence interval (Fig. 13b). Full regression reports are provided in Appendix E.

For convenience we provide an EXCEL spreadsheet for calculation of clinopyroxene-melt element-partition coefficients for any trace-element of 3+ valence that is large enough to fit onto the $\text{VI}_{\text{M}1}$ or $\text{VIII}_{\text{M}2}$ sites of clinopyroxene (Appendix F). To assess the utility of the partitioning models and to monitor for potential in-

roduction of radius-dependent bias, we show predicted REE patterns normalised to measured ratios for some literature data and our internally heated pressure vessel experiments (Fig. 14). The model accurately reproduces REE patterns at all compositions, except for HREE on the $\text{VI}_{\text{M}1}$ site of clinopyroxene at aegirine contents exceeding ~ 50 mol % (NLS experiments).

5.7. Implications for formation of REE deposits in evolved alkaline intrusions

The solubility of REE and HFSE minerals is strongly enhanced in peralkaline melts (Watson, 1979; Linnen and Keppler, 1997; Boehnke et al., 2013; Aseri et al., 2015), thus the high concentration of these elements in peralkaline systems may (partially) reflect this fact (Dostal, 2017). Melts containing high concentrations of REE and HFSE are thought to be generated through low degrees of partial melting in the mantle, followed by residual enrichment during protracted fractional crystallisation (Marks and Markl, 2017). The budget of REE and HFSE in a fractionating magma is influenced by the mineralogy of the crystallising assemblage, and the extent to which these elements are incorporated at minor or trace concentrations.

Clinopyroxene is a major ferromagnesian phase that is commonly saturated throughout the entire differentiation histories of peralkaline magmatic systems (Ablay et al., 1998; Marks and Markl, 2001; Möller and Williams-Jones, 2016). The composition of the fractionating clinopyroxene has a major impact on the absolute REE concentrations and REE pattern of the residual melt, and ultimately on the ability of a system to develop economic concentrations of the REE (Fig. 15, e.g. Kogarko, 1990; Sørensen, 1992; Marks et al., 2011). Clinopyroxene in alkaline magmatic systems is initially calcic for mafic melts, and becomes increasingly sodic as crystal fractionation proceeds (Marks et al., 2004). Although the REE are compatible in the majority of our experimentally generated clinopyroxene, those approaching aegirine end-member composition, as found in evolved alkaline magmatic systems have the lowest D_{REE} values (Fig. 6). Strongly alkaline magmatic systems are thought to crystallise abundant Ca-pyroxene early in their evolution which may deplete residual liquids with respect to REEs. Consequently, even though crystallisation of Na-pyroxene could enrich residual liquids with REE, the resultant concentration of these metals in the melt would remain low. However, clinopyroxene is not the only phase to crystallise from alkaline magmas, and the majority of additional silicate phases, such as olivine, biotite and feldspar have $D_{\text{REE}} << 1$,

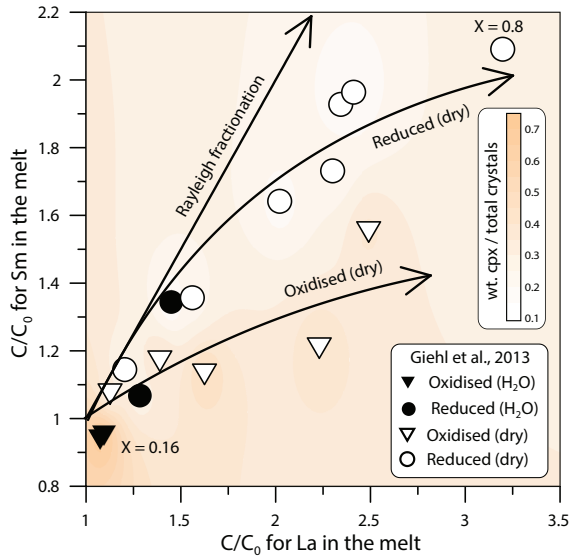


Figure 15: Model enrichment paths for La and Sm in residual melts during fractional crystallisation of a MiKa dyke composition (Gardar Province, Greenland, see Marks and Markl 2003). Phase relations and clinopyroxene compositions are from Giehl et al. (2013) and pertain to both oxidising and reducing conditions ($\log f\text{O}_2 = \Delta\text{QFM} - 3$ and +1), nominally dry to water bearing (to 3 wt.% H_2O at 1 kbar). Colour shading indicates the weight fraction of clinopyroxene within the crystallising assemblage. Bold arrows indicate residual enrichment pathways for the REE in the melt for Rayleigh fractionation (no incorporation into crystals), reduced, dry conditions, and oxidised dry conditions (the latter two are hand drawn fits to the data). For simplicity, this model does not consider REE incorporation into magnetite, alkali-feldspar, olivine, nepheline or aenigmatite, all phases generated in the experiments of Giehl et al. (2013) (see Larsen, 1979; Kovalenko et al., 1988; Mahood and Stimac, 1990).

typically 1-4 orders of magnitude lower than clinopyroxene (Larsen, 1979; Kovalenko et al., 1988; Mahood and Stimac, 1990; Fedele et al., 2015). Consequently, if the mode of clinopyroxene is low enough, the bulk D_{REE} of the crystallising assemblage would remain below unity, allowing the REE to become enriched in the residual silicate melt.

To give insight into the optimum conditions for residual magmatic enrichment of the REE in alkaline systems we modelled the evolution of REE concentrations in the melt during fractional crystallisation of a nepheline syenite body (Fig. 15). Phase relation data and clinopyroxene compositions are from the experimental study of Giehl et al. (2013). Their starting composition, based on the MiKa dyke, from the Gardar Province, Greenland, is already extremely evolved, with $\text{Mg}^{\#} = 2$, $(\text{Na} + \text{K})/\text{Al} = 1.44$ and $\text{FeO}^* = 12$ wt.-%.

In these models, crystallisation under water-bearing, oxidising conditions produces a high fraction of

clinopyroxene that depletes residual melts with respect to Sm, while subtly enriching La. Dry conditions promote abundant alkali feldspar (Afs) crystallisation, which effectively enriches the REE content of residual melts. Under oxidising, dry conditions, the La/Sm ratio of the residual melt increases with fractionation, because Sm is more effectively incorporated into clinopyroxene. Residual enrichment is most effective under dry, reducing conditions because of a relatively lower fraction of clinopyroxene within the crystallising assemblage. Because of this, the REE enrichment path of the residual melt is close to that of ideal Rayleigh fractionation. Under these reducing, dry conditions and at a temperature of 750°C, the experiments of Giehl et al. (2013) attained a crystal fraction of 0.8. Here, residual melts would have 3.2 times La concentration and 2 times the Sm concentration relative to their starting composition.

Considering these mechanisms, alongside our experimental and Canary Islands data, the best systems to develop high REE concentrations are those that would produce small proportions of Ca-pyroxene early in their crystallisation histories, quickly evolving to more sodic compositions that crystallise aegirine clinopyroxene. Cooling under low-pressure, dry, reducing conditions produces abundant alkali feldspar that in the case of a peralkaline composition, would serve to further increase the alkalinity of the residual melt. Low-degrees of source melting would produce primary melts with (1) high REE concentrations and (2) low melt Mg + Fe, and low modal abundance of clinopyroxene, which would aid enrichment in residual melts via fractional crystallisation.

The HREE-rich nature of peralkaline magmatic systems, both granites and nepheline syenites, is compatible with fractionation of moderately sodic clinopyroxene that have high $D_{\text{LREE}}/D_{\text{HREE}}$ (e.g. Möller and Williams-Jones, 2016; Dostal, 2017). As crystal fractionation progresses and clinopyroxene compositions evolve toward the aegirine end-member composition, $D_{\text{LREE}}/D_{\text{HREE}}$ decreases (Fig. 6). This systematic change in element-partitioning behaviour would result in strong HREE enrichment in aegirine-pyroxene cumulates, and would enrich the residual melt with respect to LREE-MREE.

Conclusions

- Our experiments reveal three distinct element-partitioning behaviours for Na-rich clinopyroxene that depend on aegirine content. Each of these is associated with a distinct major-element exchange

vector. We do not have the compositional resolution to know if the transition between these behaviours is smooth or step-like.

- Fits to the lattice-strain model of Blundy and Wood (1994) indicate expansion of the ^{VIII}M2 site with increasing $\text{Na}_{\text{M}2}^+$, to a maximum $r_{0,\text{M}2}^{3+}$ of 1.12 Å at $\text{Na}_{\text{M}2}^+ = 0.4$ c.f.u. Further expansion did not occur at higher Na contents.
- Both the ^{VI}M1 and ^{VIII}M2 sites of clinopyroxene shrink at high-aegirine contents in response to increasing $\sum \text{R}_{\text{M}1}^{3+}$.
- Charge effects lead to a progressive increase in $D_0^{\text{M}1}$ at the expense of $D_0^{\text{M}2}$, as the exchanges Ca^{2+} for Na^+ and M^{2+} for Fe^{3+} take place. Much like in systems of lower alkalinity, REE incorporation into clinopyroxene is dominated by coupled Al–Si substitutions at the ^{IV}T site.
- Existing predictive models for clinopyroxene/melt element-partitioning do not accurately reproduce the large ^{VIII}M2 site ($r_{0,\text{M}2}^{3+}$) of our Na-rich clinopyroxene. We have calibrated a new empirical model that may be applied to any composition between basalt and peralkaline phonolite, based on our data from experiments and natural systems, as well as a large compilation of partition coefficients from the literature.
- Crystallisation of abundant Ca-Mg rich clinopyroxene depletes the residual melts of REE, and inhibits or terminates orthomagmatic enrichment processes.
- Clinopyroxene–melt REE partitioning systematics suggest that nepheline syenites which host REE deposits must originate from low-degree melts with sufficient alkali enrichment to saturate clinopyroxene similar to our medium-aegirine clinopyroxene (Ae_{25-50}). Fractionation of such clinopyroxene enriches residual melts with respect to the HREE, in accord with the composition of REE-mineralised nepheline syenite systems.

Acknowledgements

We thank the Geo.X partners GFZ and Universität Potsdam for access to the HP-GeoMatS Lab, Don Baker for assistance with preparation of starting materials, Bruce Watson and Volker Möller for providing samples of Mud Tank zircon and the Nechalacho Layered Suite rocks, respectively, Hans Peter Nabein, Maria

Stuff and Julia Pohlenz for assistance with HP experimental equipment, Toby Soutar for help with preparation of the Canary Islands samples, Lang Shi and Glenn Poirier for assistance with electron-microprobe analyses, and Anna Jung for assistance with laser ICP-MS analyses. The manuscript benefited from discussions with Longbo Yang, Rebecca Paisley, Stephan Kolzenburg, Shane Rooyakkers and Jean Bédard. Silvio Mollo, Lorenzo Fedele and an anonymous reviewer are thanked for their insightful feedback. Nelson Eby is thanked for editorial handling. This work was funded by PhD scholarships to C.B. from Geotop, DIVEX, and the SEG Canada Foundation, and operating grants to V.v.H. and J.S. from the Natural Sciences and Engineering Research Council of Canada (grant numbers RGPIN-2014-05955, RGPAS-462335-2014) and the FQRNT team research project program.

References

- Ablay, G.J., Carroll, M.R., Palmer, M.R., Martí, J., Sparks, R.S.J., 1998. Basanite–phonolite lineages of the Teide–Pico Viejo volcanic complex, Tenerife, Canary Islands. *Journal of Petrology* 39, 905–936. doi:10.1093/petroj/39.5.905.
- Ablay, G.J., Ernst, G.G.J., Martí, J., Sparks, R.S.J., 1995. The 2 ka subplinian eruption of Montaña Blanca, Tenerife. *Bulletin of Volcanology* 57, 337–355. doi:10.1007/BF00301292.
- Adam, J., Green, T., 2006. Trace element partitioning between mica- and amphibole-bearing garnet lherzolite and hydrous basanitic melt: 1. Experimental results and the investigation of controls on partitioning behaviour. *Contributions to Mineralogy and Petrology* 152, 1–17. doi:10.1007/s00410-006-0085-4.
- Akasaka, M., Onuma, K., 1980. The join $\text{CaMgSi}_2\text{O}_6\text{-CaFeAlSi}_2\text{O}_6\text{-CaTiAl}_2\text{O}_6$ and its bearing on the Ti-rich fassaitic pyroxenes. *Contributions to Mineralogy and Petrology* 71, 301–312. doi:10.1007/BF00371672.
- Albert, H., Costa, F., Martí, J., 2015. Timing of magmatic processes and unrest associated with mafic historical monogenetic eruptions in Tenerife Island. *Journal of Petrology* 56, 1945–1966. doi:10.1093/petrology/egv058.
- Andújar, J., Scaillet, B., 2012. Experimental constraints on parameters controlling the difference in the eruptive dynamics of phonolitic magmas: the case of Tenerife (Canary Islands). *Journal of Petrology* 53, 1777–1806. doi:10.1093/petrology/egs033.
- Aseri, A.A., Linnen, R.L., Che, X.D., Thibault, Y., Holtz, F., 2015. Effects of fluorine on the solubilities of Nb, Ta, Zr and Hf minerals in highly fluxed water-saturated haplogranitic melts. *Ore Geology Reviews* 64, 736–746. doi:10.1016/j.oregeorev.2014.02.014.
- Beard, C.D., 2018. Mineral–melt trace element partitioning in alkali–lime magmatic systems. Ph.d. thesis. McGill University, Montreal, Canada.
- Bédard, J.H., 2014. Parameterizations of calcic clinopyroxene - Melt trace element partition coefficients. *Geochemistry, Geophysics, Geosystems* 15, 303–336. doi:10.1002/2013GC005112.
- Behrens, H., Hahn, M., 2009. Trace element diffusion and viscous flow in potassium-rich trachytic and phonolitic melts. *Chemical Geology* 259, 63–77. doi:10.1016/j.chemgeo.2008.10.014.
- Berndt, J., Liebske, C., Holtz, F., Freise, M., Nowak, M., Ziegenbein, D., Hurkuck, W., Koepke, J., 2002. A combined rapid-quench and H_2 -membrane setup for internally heated pres-

- sure vessels: description and application for water solubility in basaltic melts. *American Mineralogist* 87, 1717–1726. doi:10.1029/JB089iB10p08540.
- Blundy, J., Wood, B., 1994. Prediction of crystal–melt partition coefficients from elastic moduli. *Nature* 372, 452–454. doi:10.1038/372452a0.
- Blundy, J.D., Robinson, J.A.C., Wood, B.J., 1998. Heavy REE are compatible in clinopyroxene on the spinel lherzolite solidus. *Earth and Planetary Science Letters* 160, 493–504. doi:10.1016/S0012-821X(98)00106-X.
- Boehnke, P., Watson, E.B., Trail, D., Harrison, T.M., Schmitt, A.K., 2013. Zircon saturation re-revisited. *Chemical Geology* 351, 324–334. doi:10.1016/j.chemgeo.2013.05.028.
- Borchert, M., Wilke, M., Schmidt, C., Cauzid, J., Tucoulou, R., 2010. Partitioning of Ba, La, Yb and Y between haplogranitic melts and aqueous solutions: An experimental study. *Chemical Geology* 276, 225–240. doi:10.1016/j.chemgeo.2010.06.009.
- Boudreau, A.E., 2004. PALLADIUM, a program to model the chromatographic separation of the platinum-group elements, base metals and sulfur in a solidifying pile of igneous crystals. *Canadian Mineralogist* 42, 393–403. doi:10.2113/gscmin.42.2.393.
- Brown, R.J., Barry, T.L., Branney, M.J., Pringle, M.S., Bryan, S.E., 2003. The Quaternary pyroclastic succession of southeast Tenerife, Canary Islands: explosive eruptions, related caldera subsidence, and sector collapse. *Geological Magazine* 140, 265–288. doi:10.1017/S0016756802007252.
- Bryan, S.E., Martí, J., Cas, R.A.F., 1998. Stratigraphy of the Bandas del Sur Formation: an extracaldera record of Quaternary phonolitic explosive eruptions from the Las Cañadas edifice, Tenerife (Canary Islands). *Geological Magazine* 135, 605–636. doi:null.
- Carracedo, J.C., Badiola, E.R., Guillou, H., Paterne, M., Scaillet, S., Torrado, F.J.P., Paris, R., Fra-Paleo, U., Hansen, A., 2007. Eruptive and structural history of Teide Volcano and rift zones of Tenerife, Canary Islands. *Geological Society of America Bulletin* 119, 1027–1051. doi:10.1130/B26087.1.
- Carroll, M.R., Blank, J.G., 1997. The solubility of H₂O in phonolitic melts. *American Mineralogist* 82, 549–556. doi:10.1093/petrology/32.5.1021.
- Cherniak, D.J., Dimanov, A., 2010. Diffusion in pyroxene, mica and amphibole. *Reviews in Mineralogy and Geochemistry* 72, 641–690. doi:10.2138/rmg.2010.72.14.
- Chou, I.M., 1986. Permeability of precious metals to hydrogen at 2 kb total pressure and elevated temperatures. *American Journal of Science* 286, 638–658.
- Corgne, A., Wood, B.J., 2005. Trace element partitioning and substitution mechanisms in calcium perovskites. *Contributions to Mineralogy and Petrology* 149, 85–97. doi:10.1007/s00410-004-0638-3.
- Costa, F., Chakraborty, S., Dohmen, R., 2003. Diffusion coupling between major and trace elements and a model for the calculation of magma chamber residence times using plagioclase. *Geochimica et Cosmochimica Acta* 67, 2189–2200. doi:10.1016/S0016-7037(00)1345-5.
- Coumans, J.P., Stix, J., Clague, D.A., Minarik, W.G., Layne, G.D., 2016. Melt-rock interaction near the Moho: Evidence from crystal cargo in lavas from near-ridge seamounts. *Geochimica et Cosmochimica Acta* 191, 139–164. doi:10.1016/j.gca.2016.07.017.
- Deer, W.A., Howie, R.A., Zussman, J., 1992. An introduction to the rock-forming minerals. Longman Group Ltd, New York.
- Dostal, J., 2017. Rare earth element deposits of alkaline igneous rocks. *Resources* 6, 1–12. doi:10.3390/resources6030034.
- Downes, H., Balaganskaya, E., Beard, A., Lifervich, R., Demaiffe, D., 2005. Petrogenetic processes in the ultramafic, alkaline and carbonatitic magmatism in the Kola Alkaline Province: A review. *Lithos* 85, 48–75. doi:10.1016/j.lithos.2005.03.020.
- Droop, G.T.R., 1987. A general equation for estimating Fe³⁺ concentrations in ferromagnesian silicates and oxides from microprobe analyses, using stoichiometric criteria. *Mineralogical magazine* 51, 431–435.
- Dygert, N., Liang, Y., Sun, C., Hess, P., 2014. An experimental study of trace element partitioning between augite and Fe-rich basalts. *Geochimica et Cosmochimica Acta* 132, 170–186. doi:10.1016/j.gca.2014.01.042.
- Edgar, C.J., Wolff, J.A., Olin, P.H., Nichols, H.J., Pittari, A., Cas, R.A.F., Reiners, P.W., Spell, T.L., Martí, J., 2007. The late Quaternary Diego Hernandez Formation, Tenerife: Volcanology of a complex cycle of voluminous explosive phonolitic eruptions. *Journal of Volcanology and Geothermal Research* 160, 59–85. doi:10.1016/j.jvolgeores.2006.06.001.
- Eugster, H.P., Wones, D.R., 1962. Stability relations of the ferruginous biotite, annite. *Journal of Petrology* 3, 82–125. doi:10.1093/petrology/3.1.182.
- Fedele, L., Lustrino, M., Melluso, L., Morra, V., Zanetti, A., Vanucci, R., 2015. Trace-element partitioning between plagioclase, alkali feldspar, Ti-magnetite, biotite, apatite, and evolved potassic liquids from Campi Flegrei (Southern Italy). *American Mineralogist* 100, 233–249. doi:10.2138/am-2015-4995.
- Fedele, L., Zanetti, A., Morra, V., Lustrino, M., Melluso, L., Vanucci, R., 2009. Clinopyroxene/liquid trace element partitioning in natural trachyte-trachyphonolite systems: insights from Campi Flegrei (southern Italy). *Contributions to Mineralogy and Petrology* 158, 337–356. doi:10.1007/s00410-009-0386-5.
- Foley, S.F., Prelevic, D., Rehfeldt, T., Jacob, D.E., 2013. Minor and trace elements in olivines as probes into early igneous and mantle melting processes. *Earth and Planetary Science Letters* 363, 181–191. doi:10.1016/j.epsl.2012.11.025.
- Francis, D., Minarik, W., 2008. Aluminum-dependent trace element partitioning in clinopyroxene. *Contributions to Mineralogy and Petrology* 156, 439–451. doi:10.1007/s00410-008-0295-z.
- Gaetani, G.A., 2004. The influence of melt structure on trace element partitioning near the peridotite solidus. *Contributions to Mineralogy and Petrology* 147, 511–527. doi:10.1007/s00410-004-0575-1.
- Gaetani, G.A., Grove, T.L., 1995. Partitioning of rare earth elements between clinopyroxene and silicate melt: Crystal-chemical controls. *Geochimica et Cosmochimica Acta* 59, 1951–1962. doi:10.1016/0016-7037(95)00119-0.
- Gaillard, F., Scaillet, B., Pichavant, M., 2002. Kinetics of iron oxidation-reduction in hydrous silicic melts. *American Mineralogist* 87, 829–837. doi:10.2138/am-2002-0704.
- Giehl, C., Marks, M., Nowak, M., 2013. Phase relations and liquid lines of descent of an iron-rich peralkaline phonolitic melt: an experimental study. *Contributions to Mineralogy and Petrology* 165, 283–304. doi:10.1007/s00410-012-0809-6.
- Giordano, D., Nichols, A., Dingwell, D., 2005. Glass transition temperatures of natural hydrous melts: a relationship with shear viscosity and implications for the welding process. *Journal of Volcanology and Geothermal Research* 142, 105–118. doi:10.1016/j.jvolgeores.2004.10.015.
- Girnis, A.V., Bulatov, V.K., Brey, G.P., Gerdes, A., Höfer, H.E., 2013. Trace element partitioning between mantle minerals and silico-carbonate melts at 6–12 GPa and applications to mantle metasomatism and kimberlite genesis. *Lithos* 160–161, 183–200. doi:10.1016/j.lithos.2012.11.027.
- Goodenough, K.M., Schilling, J., Jonsson, E., Kalvig, P., Charles, N., Tuduri, J., Deady, E.A., Sadeghi, M., Schiellerup, H., Müller, A., Bertrand, G., Arvanitidis, N., Eliopoulos, D.G., Shaw, R.A., Thrane, K., Keulen, N., 2016. Europe's rare earth element resource potential: An overview of REE metallogenetic provinces and their geodynamic setting. *Ore Geology Reviews* 72, 838–856. doi:10.1016/j.oregeorev.2015.09.019.

- 1361 Grove, T.L., Baker, M.B., Kinzler, R.J., 1984. Coupled CaAl-NaSi 1426
 1362 diffusion in plagioclase feldspar: Experiments and applications to 1427
 1363 cooling rate speedometry. *Geochimica et Cosmochimica Acta* 48, 1428
 1364 2113–2121. doi:10.1016/0016-7037(84)90391-0. 1429
- 1365 Guillou, H., Carracedo, J.C., Paris, R., Pérez Torrado, F.J., 2004. 1430
 1366 Implications for the early shield-stage evolution of Tenerife from 1431
 1367 K/Ar ages and magnetic stratigraphy. *Earth and Planetary Science 1432
 Letters* 222, 599–614. doi:10.1016/j.epsl.2004.03.012. 1433
- 1368 Gurendo, A.A., Hoernle, K.A., Hauff, F., Schmincke, H.U., Han, 1434
 1369 D., Miura, Y.N., Kaneoka, I., 2006. Major, trace element 1435
 1370 and NdSrPbOHeAr isotope signatures of shield stage lavas from 1436
 1371 the central and western Canary Islands: Insights into man- 1437
 1372 tle and crustal processes. *Chemical Geology* 233, 75–112. 1438
 1373 doi:10.1016/j.chemgeo.2006.02.016. 1439
- 1374 Hanchar, J.M., Finch, R.J., Hoskin, P.W.O., Watson, E.B., Cherniak, 1440
 1375 D.J., Mariano, A.N., 2001. Rare earth elements in synthetic zir- 1441
 1376 con: Part 1. Synthesis, and rare earth element and phosphorus 1442
 1377 doping. *American Mineralogist* 86, 667–680. doi:10.1130/0091- 1443
 1378 7613(1990)018;0757:CTOGAS;2.3.CO;2. 1444
- 1379 Hazen, R.M., Finger, L.W., 1979. Bulk modulus-volume relation- 1445
 1380 ship for cation-anion polyhedra. *Journal of Geophysical Research:* 1446
 1381 *Solid Earth* 84, 6723–6728. doi:10.1029/JB084iB12p06723. 1447
- 1382 Hill, E., Blundy, J.D., Wood, B.J., 2011. Clinopyroxene-melt trace 1448
 1383 element partitioning and the development of a predictive model 1449
 1384 for HFSE and Sc. *Contributions to Mineralogy and Petrology* 161, 1450
 1385 423–438. doi:10.1007/s00410-010-0540-0. 1451
- 1386 Hill, E., Wood, B.J., Blundy, J.D., 2000. The effect of Ca-Tschermaks 1452
 1387 component on trace element partitioning between clinopyroxene 1453
 1388 and silicate melt. *Lithos* 53, 203–215. doi:10.1016/S0024- 1454
 1389 4937(00)00025-6. 1455
- 1390 Huang, F., Lundstrom, C.C., McDonough, W.F., 2006. Effect of 1456
 1391 melt structure on trace-element partitioning between clinopyrox- 1457
 1392 ene and silicic, alkaline, aluminous melts. *American Mineralogist* 1458
 1393 91, 1385–1400. doi:10.2138/am.2006.1909. 1459
- 1394 Jugó, P.J., Wilke, M., Botcharnikov, R.E., 2010. Sulfur K-edge 1460
 1395 XANES analysis of natural and synthetic basaltic glasses: Im- 1461
 1396 plications for S speciation and S content as function of oxygen 1462
 1397 fugacity. *Geochimica et Cosmochimica Acta* 74, 5926–5938. 1463
 1398 doi:10.1016/j.gca.2010.07.022. 1464
- 1399 Kennedy, A.K., Lofgren, G.E., Wasserburg, G.J., 1993. An exper- 1465
 1400 imental study of trace element partitioning between olivine, or- 1466
 1401 thopyroxene and melt in chondrules: equilibrium values and ki- 1467
 1402 netic effects. *Earth and Planetary Science Letters* 115, 177–195. 1468
 1403 doi:10.1016/0012-821X(93)90221-T. 1469
- 1404 Kogarko, L.N., 1990. Ore-forming potential of alkaline magmas. 1470
 1405 *Lithos* 26, 167–175. doi:10.1016/0024-4937(90)90046-4. 1471
- 1406 Kovalenko, V.I., Hervig, R.L., Sheridan, M.F., 1988. Ion microprobe 1472
 1407 analyses of trace elements in anorthoclase, hedenbergite, aenig- 1473
 1408 matite, quartz, apatite and glass in pantellerite: evidence for high 1474
 1409 water contents in pantellerite melt. *American Mineralogist* 73, 1475
 1410 1038–1045. 1476
- 1411 Kress, V.C., Carmichael, I.S.E., 1991. The compressibility of 1477
 1412 silicate liquids containing Fe₂O₃ and the effect of composi- 1478
 1413 tion, temperature, oxygen fugacity and pressure on their redox 1479
 1414 states. *Contributions to Mineralogy and Petrology* 108, 82–92. 1480
 1415 doi:10.1007/BF00307328. 1481
- 1416 Kumazawa, M., 1969. The elastic constants of single-crystal or- 1482
 1417 thopyroxene. *Journal of Geophysical Research* 74, 5973–5980. 1483
 1418 doi:10.1029/JB074i025p05973. 1484
- 1419 Larsen, L.M., 1979. Distribution of REE and other trace elements 1485
 1420 between phenocrysts and peralkaline undersaturated magmas, ex- 1486
 1421 emplified by rocks from the Gardar igneous province, south Green- 1487
 1422 land. *Lithos* 12, 303–315. doi:10.1016/0024-4937(79)90022-7. 1488
- 1423 Law, K.M., Blundy, J.D., Wood, B.J., Ragnarsdottir, K.V., 1489
 1424 2000. Trace element partitioning between wollastonite and 1490
 1425 silicate-carbonate melt. *Mineralogical Magazine* 64, 651–661.
 doi:10.1180/002646100549670.
- 1426 Le Bas, M.J., Le Maitre, R.W., Streckeisen, A., Zanettin, B., 1986.
 1427 A Chemical Classification of Volcanic Rocks Based on the Total
 1428 Alkali-Silica Diagram. *Journal of Petrology* 27, 745–750.
 doi:10.1093/petrology/27.3.745.
- 1429 Liang, Y., Richter, F.M., Watson, E.B., 1994. Convection in multi- 1430
 1431 component silicate melts driven by coupled diffusion. *Nature* 369,
 1432 390–392. doi:10.1038/369390a0.
- 1433 Linnen, R.L., Keppler, H., 1997. Columbite solubility in granitic 1434
 1435 melts: consequences for the enrichment and fractionation of Nb 1436
 1437 and Ta in the Earth's crust. *Contributions to Mineralogy and Petrology* 128, 213–227. doi:10.1007/s004100050304.
- 1438 Lofgren, G., 1989. Dynamic crystallization of chondrule melts 1439
 1440 of porphyritic olivine composition: Textures experimental and 1441
 1442 natural. *Geochimica et Cosmochimica Acta* 53, 461–470.
 doi:10.1016/0016-7037(89)90397-9.
- 1443 Lofgren, G.E., Huss, G.R., Wasserburg, G.J., 2006. An ex- 1444
 1445 perimental study of trace-element partitioning between Ti-Al- 1446
 1447 clinopyroxene and melt: Equilibrium and kinetic effects in- 1448
 1449 cluding sector zoning. *American Mineralogist* 91, 1596–1606.
 doi:10.2138/am.2006.2108.
- 1450 Lu, F., Anderson, A.T., Davis, A.M., 1995. Diffusional gradients at 1451
 1452 the crystal / melt interface and their effect on the compositions of 1453
 1454 melt inclusions. *The Journal of Geology* 103, 591–597.
- 1455 Lundstrom, C.C., Shaw, H.F., Ryerson, F.J., Phinney, D.L., Gill, 1456
 1457 J.B., Williams, Q., 1994. Compositional controls on the parti- 1458
 1459 tioning of U, Th, Ba, Pb, Sr and Zr between clinopyroxene and 1460
 1461 haplobasaltic melts: implications for uranium series disequilibria 1462
 1462 in basalts. *Earth and Planetary Science Letters* 128, 407–423.
 doi:10.1016/0012-821X(94)90159-7.
- 1463 Mahood, G.A., Stimac, J.A., 1990. Trace-element partitioning in pan- 1464
 1464 tellerites and trachytes. *Geochimica et Cosmochimica Acta* 54,
 1465 2257–2276. doi:10.1016/0016-7037(90)90050-U.
- 1466 Marks, M., Halama, R., Wenzel, T., Markl, G., 2004. Trace el- 1467
 1467 ement variations in clinopyroxene and amphibole from alkaline 1468
 1468 to peralkaline syenites and granites: implications for mineral- 1469
 1469 melt trace-element partitioning. *Chemical Geology* 211, 185–215.
 doi:10.1016/j.chemgeo.2004.06.032.
- 1470 Marks, M., Markl, G., 2001. Fractionation and assimilation processes 1471
 1471 in the alkaline augite syenite unit of the Ilímaussaq intrusion, south 1472
 1472 Greenland, as deduced from phase equilibria. *Journal of Petrology* 42, 1473
 1473 1947–1969. doi:10.1093/petrology/42.10.1947.
- 1474 Marks, M., Markl, G., 2003. Ilímaussaq en miniature': closed- 1475
 1475 system fractionation in an aegapitic dyke rock from the Gar- 1476
 1476 dar Province, South Greenland (contribution to the mineralogy 1477
 1477 of Ilímaussaq no. 117). *Mineralogical Magazine* 67, 893–919.
 doi:10.1180/0026461036750150.
- 1478 Marks, M.A., Markl, G., 2017. A global review on a- 1479
 1479 gapitic rocks. *Earth-Science Reviews* 173, 229–258.
 doi:10.1016/j.earscirev.2017.06.002.
- 1480 Marks, M.A.W., Hettmann, K., Schilling, J., Frost, B.R., Markl, 1481
 1481 G., 2011. The mineralogical diversity of alkaline igneous 1482
 1482 rocks: Critical factors for the transition from miaskitic to a- 1483
 1483 gapitic phase assemblages. *Journal of Petrology* 52, 439–455.
 doi:10.1093/petrology/egg086.
- 1484 Möller, V., Williams-Jones, A.E., 2016. Petrogenesis of the Nechal- 1485
 1485 cho Layered Suite, Canada: magmatic Evolution of a REE-Nb-rich 1486
 1486 Nepheline Syenite Intrusion. *Journal of Petrology* 57, 229–276.
 doi:10.1093/petrology/egw003.
- 1487 Mollo, S., Blundy, J.D., Giacomoni, P., Nazzari, M., Scar- 1488
 1488 lato, P., Coltorti, M., Langone, A., Andronico, D., 2017. 1489
 1489 Clinopyroxene-melt element partitioning during interaction be- 1490
 1490 tween trachybasaltic magma and siliceous crust: Clues from 1491
 1491 quartzite enclaves at Mt. Etna volcano. *Lithos* 284–285, 447–461.

- doi:10.1016/j.lithos.2017.05.003.

Mollo, S., Blundy, J.D., Iezzi, G., Scarlato, P., Langone, A., 2013. The partitioning of trace elements between clinopyroxene and trachybasaltic melt during rapid cooling and crystal growth. *Contributions to Mineralogy and Petrology* 166, 1633–1654. doi:10.1007/s00410-013-0946-6.

Mollo, S., Forni, F., Bachmann, O., Blundy, J.D., De Astis, G., Scarlato, P., 2016. Trace element partitioning between clinopyroxene and trachy-phonolitic melts: A case study from the Campagnano Ignimbrite (Campi Flegrei, Italy). *Lithos* 252/253, 160–172. doi:10.1016/j.lithos.2016.02.024.

Moore, G., Vennemann, T., Carmichael, I.S.E., 1998. An empirical model for the solubility of H₂O in magmas to 3 kilobars. *American Mineralogist* 83, 36–42. doi:10.1016/0012-821X(73)90129-5.

Morimoto, N., 1989. Nomenclature of pyroxenes. *Mineralogical Journal* 14, 198–221. doi:10.2465/minerj.14.198.

Mungall, J., Brenan, J., 2014. Partitioning of platinum-group elements and Au between sulfide liquid and basalt and the origins of mantle-crust fractionation of the chalcophile elements. *Geochimica et Cosmochimica Acta* 125, 265–289. doi:10.1016/j.gca.2013.10.002.

Mysen, B.O., Virgo, D., Seifert, F.A., 1982. The structure of silicate melts: Implications for chemical and physical properties of natural magma. *Reviews of Geophysics* 20, 353–383. doi:10.1029/RG020i003p00353.

Mysen, B.O., Virgo, D., Seifert, F.A., 1985. Relationships between properties and structure of aluminosilicate melts. *American Mineralogist* 70, 88–105. doi:10.1007/BF00413348.

Niu, Y., 2004. Bulk-rock major and trace element compositions of abyssal peridotites: Implications for mantle melting, melt extraction and post-melting processes beneath Mid-Ocean ridges. *Journal of Petrology* 45, 2423–2458. doi:10.1093/petrology/egh068.

Olin, P.H., Wolff, J.A., 2010. Rare earth and high field strength element partitioning between iron-rich clinopyroxenes and felsic liquids. *Contributions to Mineralogy and Petrology* 160, 761–775. doi:10.1007/s00410-010-0506-2.

Onuma, N., Higuchi, H., Wakita, H., Nagasawa, H., 1968. Trace element partition between two pyroxenes and the host lava. *Earth and Planetary Science Letters* 5, 47–51. doi:10.1016/S0012-821X(68)80010-X.

Paton, C., Hellstrom, J., Paul, B., Woodhead, J., Hergt, J., 2011. Iolite: Freeware for the visualisation and processing of mass spectrometric data. *Journal of Analytical Atomic Spectrometry* 26, 2508–2518. doi:10.1039/C1JA10172B.

Peters, S.T., Troll, V.R., Weis, F.A., Dallai, L., Chadwick, J.P., Schulz, B., 2017. Amphibole megacrysts as a probe into the deep plumbing system of Merapi volcano, Central Java, Indonesia. *Contributions to Mineralogy and Petrology* 172, 1–20. doi:10.1007/s00410-017-1338-0.

Putirka, K.D., 2008. Thermometers and Barometers for Volcanic Systems. *Reviews in Mineralogy and Geochemistry* 69, 61–120. doi:10.2138/rmg.2008.69.3.

Rapp, R.P., Watson, E.B., 1986. Monazite solubility and dissolution kinetics: implications for the thorium and light rare earth chemistry of felsic magmas. *Contributions to Mineralogy and Petrology* 94, 304–316. doi:10.1007/BF00371439.

Rasband, W., 2016. ImageJ. U.S. National Institutes of Health, Bethesda, Maryland, USA.

Redhammer, G.J., Amthauer, G., Roth, G., Tippelt, G., Lottermoser, W., 2006. Single-crystal X-ray diffraction and temperature dependent 57Fe Mössbauer spectroscopy on the hedenbergite-aegirine (Ca,Na)(Fe₂₊,Fe₃₊)Si₂O₆ solid solution. *American Mineralogist* 91, 1271–1292. doi:10.2138/am.2006.2173.

Reguir, E.P., Chakhmouradian, A.R., Pisik, L., Halden, N.M., Yang, P., Xu, C., Kynický, J., Couëslen, C.G., 2012. Trace-element com-

position and zoning in clinopyroxene- and amphibole-group minerals: Implications for element partitioning and evolution of carbonatites. *Lithos* 128, 27–45. doi:10.1016/j.lithos.2011.10.003.

Rubatto, D., Hermann, J., 2007. Experimental zircon/melt and zircon/garnet trace element partitioning and implications for the geochronology of crustal rocks. *Chemical Geology* 241, 38–61. doi:10.1016/j.chemgeo.2007.01.027.

Schmidt, B.C., Behrens, H., 2008. Water solubility in phonolite melts: Influence of melt composition and temperature. *Chemical Geology* 256, 259–268. doi:10.1016/j.chemgeo.2008.06.043.

Schmidt, K.H., Bottazzi, P., Vannucci, R., Mengel, K., 1999. Trace element partitioning between phlogopite, clinopyroxene and leucite lampreite melt. *Earth and Planetary Science Letters* 168, 287–299. doi:10.1016/S0012-821X(99)00056-4.

Schmidt, M.W., Connolly, J.A.D., Günther, D., Bogaerts, M., 2006. Element partitioning: The role of melt structure and composition. *Science* 312, 1646–1650. doi:10.1126/science.1126690.

Severs, M.J., Beard, J.S., Fedele, L., Hanchar, J.M., Mutchler, S.R., Bodnar, R.J., 2009. Partitioning behavior of trace elements between dacitic melt and plagioclase, orthopyroxene, and clinopyroxene based on laser ablation ICPMS analysis of silicate melt inclusions. *Geochimica et Cosmochimica Acta* 73, 2123–2141. doi:10.1016/j.gca.2009.01.009.

Shannon, R., 1976. Revised effective ionic radii and systematic studies of interatomic distances in halides and chalcogenides. *Acta Crystallographica Section A* 32, 751–767.

Shea, T., Hammer, J.E., 2013. Kinetics of cooling- and decompression-induced crystallization in hydrous mafic-intermediate magmas. *Journal of Volcanology and Geothermal Research* 260, 127–145. doi:10.1016/j.jvolgeores.2013.04.018.

Shearer, C.K., Larsen, L.M., 1994. Sector-zoned aegirine from the Ilmaussaq alkaline intrusion, South Greenland; implications for trace-element behavior in pyroxene. *American Mineralogist* 79, 340–352.

Sjöqvist, A., Cornell, D., Andersen, T., Erambert, M., Ek, M., Leijd, M., 2013. Three compositional varieties of rare-earth element ore: Eudialyte-group minerals from the Norra Kärr alkaline complex, Southern Sweden. *Minerals* 3, 94–120. doi:10.3390/min3010094.

Sørensen, H., 1992. Agpaitic nepheline syenites: a potential source of rare elements. *Applied Geochemistry* 7, 417–427. doi:10.1016/0883-2927(92)90003-L.

Spera, F.J., Bohrson, W.A., 2001. Energy-constrained open-system magmatic processes I: General model and energy-constrained assimilation and fractional crystallization (EC-AFC) formulation. *Journal of Petrology* 42, 999–1018. doi:10.1093/petrology/42.5.999.

Stevens, J., 1996. Applied multivariate analysis for the social sciences. Lawrence Erlbaum, Mahwah, NJ.

Sun, C., Liang, Y., 2012. Distribution of REE between clinopyroxene and basaltic melt along a mantle adiabat: Effects of major element composition, water, and temperature. *Contributions to Mineralogy and Petrology* 163, 807–823. doi:10.1007/s00410-011-0700-x.

Thirlwall, M.F., Singer, B.S., Marriner, G.F., 2000. 39Ar–40Ar ages and geochemistry of the basaltic shield stage of Tenerife, Canary Islands, Spain. *Journal of Volcanology and Geothermal Research* 103, 247–297. doi:10.1016/S0377-0273(00)00227-4.

Troll, V., Schmincke, H., 2002. Magma mixing and crustal recycling recorded in ternary feldspar from compositionally zoned peralkaline ignimbrite 'A', Gran Canaria, Canary Islands. *Journal of Petrology* 43, 243–270. doi:10.1093/petrology/43.2.243.

Van Orman, J.A., Grove, T.L., Shimizu, N., 2001. Rare earth element diffusion in diopside: influence of temperature, pressure, and ionic radius, and an elastic model for diffusion in silicates. *Contributions to Mineralogy and Petrology* 141, 687–703. doi:10.1007/s004100100269.

- 1621 Walker, D., Kirkpatrick, R.J., Longhi, J., Hays, J.F., 1976. Crystallization history of lunar picritic basalt sample 12002: Phase-equilibria and cooling-rate studies. *Bulletin of the Geological Society of America* 87, 646–656. doi:10.1130/0016-7606.
- 1622 Watson, E.B., 1979. Zircon saturation in felsic liquids: Experimental results and applications to trace element geochemistry. *Contributions to Mineralogy and Petrology* 70, 407–419. doi:10.1007/BF00371047.
- 1623 Weidner, D.J., Vaughan, M.T., 1982. Elasticity of pyroxenes: Effects of composition versus crystal structure. *Journal of Geophysical Research* 87, 9349–9353.
- 1624 Wiesmaier, S., Troll, V.R., Carracedo, J.C., Ellam, R.M., Bindeman, I., Wolff, J.A., 2012. Bimodality of lavas in the Teide–Pico Viejo Succession in Tenerife—the role of crustal melting in the origin of recent phonolites. *Journal of Petrology* 53, 2465–2495. doi:10.1093/petrology/egs056.
- 1625 Wood, B.J., Blundy, J.D., 1997. A predictive model for rare earth element partitioning between clinopyroxene and anhydrous silicate melt. *Contributions to Mineralogy and Petrology* 129, 166–181. doi:10.1007/s004100050330.
- 1626 Wood, B.J., Blundy, J.D., 2001. The effect of cation charge on crystal–melt partitioning of trace elements. *Earth and Planetary Science Letters* 188, 59–71. doi:10.1016/S0012-821X(01)00294-1.
- 1627 Wood, B.J., Blundy, J.D., 2003. Trace element partitioning under crustal and uppermost mantle conditions: The influences of ionic radius, cation charge, pressure, and temperature, in: Carlson, R.W. (Ed.), *The Mantle and Core: Treatise on Geochemistry*. Elsevier. volume 2. chapter 2.09, pp. 395–424. doi:10.1016/B0-08-043751-6/02009-0.
- 1628 Wood, B.J., Blundy, J.D., 2014. Trace element partitioning: The influences of ionic radius, cation charge, pressure, and temperature, in: Carlson, R.W. (Ed.), *The Mantle and Core: Treatise on Geochemistry: Second Edition*. Elsevier. chapter 3.11, pp. 421–445. doi:10.1016/B978-0-08-095975-7.00206-0.
- 1629 Wood, B.J., Trigila, R., 2001. Experimental determination of aluminous clinopyroxene–melt partition coefficients for potassic liquids, with application to the evolution of the Roman province potassic magmas. *Chemical Geology* 172, 213–223. doi:10.1016/S0009-2541(00)00259-X.
- 1630 Workman, R.K., Hart, S.R., 2005. Major and trace element composition of the depleted MORB mantle (DMM). *Earth and Planetary Science Letters* 231, 53–72. doi:10.1016/j.epsl.2004.12.005.
- 1631 Wörner, G., Beusen, J.M., Duchateau, N., Gijbels, R., Schmincke, H.U., 1983. Trace element abundances and mineral/melt distribution coefficients in phonolites from the Laacher See volcano (Germany). *Contributions to Mineralogy and Petrology* 84, 152–173. doi:10.1007/BF00371282.
- 1632 Xu, C., Kynicky, J., Chakhmouradian, A.R., Campbell, I.H., Allen, C.M., 2010. Trace-element modeling of the magmatic evolution of rare-earth-rich carbonatite from the Miaoya deposit, Central China. *Lithos* 118, 145–155. doi:10.1016/j.lithos.2010.04.003.
- 1633 Yang, L., van Hinsberg, V.J., Samson, I., 2018. A new method to deconvolute binary mixture in LA-ICP-MS analyses to quantify the composition of phases smaller than the laser spot size. *Journal of Analytical Atomic Spectrometry* 33, 1518–1528. doi:10.1039/C8JA00078F.
- 1634 Yao, L., Sun, C., Liang, Y., 2012. A parameterized model for REE distribution between low-Ca pyroxene and basaltic melts with applications to REE partitioning in low-Ca pyroxene along a mantle adiabat and during pyroxenite-derived melt and peridotite interaction. *Contributions to Mineralogy and Petrology* 164, 261–280. doi:10.1007/s00410-012-0737-5.
- 1635 Zhang, Y., Ni, H., Chen, Y., 2010. Diffusion data in silicate melts. *Reviews in Mineralogy and Geochemistry* 72, 311–408. doi:10.2138/rmg.2010.72.8.

1686 **6. Tables**

Table 1: Major-element composition (in wt%) of starting materials for the internally heated pressure vessel experiments. The totals are calculated with all iron as FeO.

Dry starting glass compositions calculated from masses of reagents added [wt%]										
Composition	SiO ₂	TiO ₂	Al ₂ O ₃	FeOT	MgO	CaO	Na ₂ O	K ₂ O	Total	(Na+K)/Al
L4	57.48	1.50	19.00	5.89	1.61	3.21	7.33	3.98	100.00	0.861
L5	61.24	0.68	19.51	3.77	0.43	0.91	8.63	4.84	100.00	0.996
M3	52.67	2.27	18.13	7.86	2.75	5.40	7.19	3.73	100.00	0.875
M4	56.35	1.47	18.63	5.77	1.58	3.15	8.48	4.57	100.00	1.014
M5	60.04	0.66	19.13	3.69	0.42	0.89	9.76	5.41	100.00	1.145
H4	54.80	1.43	18.12	5.62	1.54	3.06	10.07	5.38	100.00	1.236
H5	58.38	0.65	18.60	3.59	0.41	0.86	11.31	6.20	100.00	1.362

Water saturated glass compositions from superliquidus experiments (EPMA) [wt%]										
	57.46	0.643	16.59	2.363	0.404	0.985	7.840	4.462	90.75	1.069
s.d. (n = 8)	0.299	0.087	0.210	0.059	0.035	0.050	0.175	0.132	0.351	0.017
rsd	0.52%	13.58%	1.26%	2.51%	8.70%	5.09%	2.23%	2.97%	0.39%	1.57%
H5	55.58	0.612	16.21	2.568	0.422	0.906	10.77	5.732	92.80	1.476
s.d. (n = 13)	0.327	0.057	0.221	0.113	0.044	0.049	0.205	0.154	0.417	0.028
rsd	0.59%	9.33%	1.36%	4.41%	10.44%	5.40%	1.90%	2.69%	0.45%	1.87%

Table 2: Summary of run conditions and run products for the internally-heated pressure vessel experiments.

Experiment	Setup	Pressure [bar]	Cooling ramp			TE-1/TE-3 [°C]	TE-2 (spl) [°C]	Time (after ramp) [h,m]	Run products
			Rate °C /min	Cycle +10°C					
L4 ₃	IHPV RQ (f)	2038	1	Y	825	828	44h50m	Cpx + Ox + Ttn + Melt	
L5 ₃	IHPV RQ (f)	2038	1	Y	825	828	44h50m	Cpx + Ox + Melt	
M3 ₂	IHPV RQ	2020	1	Y	796/795	799	47h	Cpx + Ox + Bt + Melt	
M4 ₄	IHPV RQ	2020	1	Y	796/795	799	47h	Cpx + Ox + Bt + Melt	
M5	IHPV	2000	-	-	800	799	47h55m	Cpx + Bt + Fsp + Melt	
M5 ₂	IHPV RQ	2000	-	-	700	689	45h45m	Cpx + Bt + Fsp + Melt	
H4 ₂	IHPV	2000	-	-	800	799	47h55m	Cpx + Ttn + Melt	
H5 ₂	IHPV RQ	2000	-	-	700	689	45h45m	Cpx + Bt + Fsp + Melt	
H5 ₃	IHPV RQ	2020	-	-	651/649	648	46h15m	Cpx + Bt + Fsp + Melt	
NLS-9	IHPV RQ	2020	1	Y	651/649	648	46h15m	Cpx + Ox + Melt	
NLS-9 ₂ HM	IHPV RQ**	2000	1	Y	650	655	42h	Cpx + Ox + Fsp + Melt	

(f) indicates failure of the rapid quench apparatus; ** indicates use of a haematite double capsule, for run conditions at the haematite-magnetite fO₂ buffer (Eugster and Wones, 1962). Cpx = clinopyroxene; Ox = spinel oxide; Ttn = titanite; Bt = biotite; Fsp = sanidine feldspar.

Table 3: Representative major-element compositions of clinopyroxene and melt for the performed internally heated pressure vessel experiments and Canary Islands phenocryst–glass pairs.

Clinopyroxene	L4 ₃	M3 ₂	M5 ₂	H5 ₃	NLS-9	NLS-9 ₂ <i>HM</i>	16-07 LMB	17-12 M. Samara	17-14 UMB-II	21-30 PV 2 ka
SiO ₂	44.70	40.73	47.31	46.95	50.73	51.90	52.43	51.77	51.81	52.50
TiO ₂	3.07	4.57	3.17	4.47	0.10	0.10	0.80	0.78	0.74	0.75
Al ₂ O ₃	5.23	9.26	3.08	3.10	2.46	2.96	1.33	1.24	1.27	1.22
FeO	13.31	11.72	18.84	16.95	28.14	28.61	9.71	9.62	10.51	10.02
MnO	0.01	0.01	0.01	0.00	0.25	0.17	0.78	0.84	0.91	0.81
MgO	9.09	9.28	5.55	6.05	0.05	0.07	12.30	12.64	12.07	11.88
CaO	19.49	22.17	16.11	15.29	5.88	3.14	21.90	21.76	21.52	22.02
Na ₂ O	2.27	1.01	4.34	4.97	9.86	11.45	1.18	1.17	1.38	1.19
K ₂ O	0.09	0.03	0.08	0.07	0.04	0.04	0.02	0.03	0.00	0.02
Total	97.25	98.78	98.49	97.85	97.49	98.45	100.44	99.85	100.22	100.42
<i>Glass</i>										
SiO ₂	58.79	57.29	57.45	54.91	58.17	58.14	60.38	55.10	59.08	60.04
TiO ₂	0.35	0.27	0.23	0.62	0.00	0.00	0.64	1.73	0.66	0.66
Al ₂ O ₃	17.35	19.14	16.69	16.06	18.55	19.41	19.96	18.30	19.68	19.79
Fe ₂ O ₃ (T)	2.35	1.35	1.01	3.16	1.67	1.91	3.65	7.22	4.02	3.96
FeO(T)	2.12	1.22	0.91	2.84	1.50	1.72	3.28	6.49	3.62	3.56
MnO	0.02	0.00	-	0.01	0.06	0.04	0.14	0.23	0.22	0.20
MgO	0.20	0.13	0.15	0.35	0.00	0.00	0.39	1.84	0.32	0.35
CaO	0.55	0.95	0.24	0.84	0.23	0.23	0.76	4.10	0.77	0.74
Na ₂ O	7.17	7.32	9.08	8.88	11.12	9.80	9.00	7.26	9.76	9.05
K ₂ O	4.68	4.10	4.68	5.30	1.51	2.51	5.41	4.09	5.45	5.57
Total	91.23	90.41	89.43	89.81	91.15	91.85	99.95	99.13	99.56	99.95
(Na+K)/Al	0.97	0.86	1.15	1.27	1.07	0.97	1.01	1.12	1.09	1.09

Table 4: Clinopyroxene–melt trace-element-partition coefficients for representative experiments and a natural phenocryst–glass pair.

-	L4 ₃		M3 ₂		M5 ₂		H5 ₃		NLS-9		NLS-9 ₂ <i>HM</i>		16-07-px4 LMB	
	D	σ	D	σ	D	σ	D	σ	D	σ	D	σ	D	σ
Li	0.250	0.016	0.126	0.009	0.419	0.034	0.427	0.024	0.274	0.029	0.251	0.025	0.157	0.021
Ga	0.364	0.022	0.567	0.020	0.190	0.022	-	-	-	-	-	-	0.216	0.020
Rb	0.005	0.002	0.018	0.003	0.010	0.006	0.013	0.002	0.026	0.015	-	-	0.000	0.000
Sr	0.828	0.045	0.282	0.024	1.433	0.111	0.997	0.091	0.321	0.045	0.269	0.111	0.732	0.293
Y	5.577	0.302	13.784	1.949	1.814	0.236	1.102	0.060	0.482	0.048	0.713	0.070	2.183	0.232
Zr	1.699	0.082	2.537	0.222	1.361	0.089	1.164	0.083	2.102	0.196	3.895	0.482	0.434	0.047
Nb	0.126	0.085	0.889	0.258	0.554	0.280	1.688	0.196	2.382	0.294	9.642	4.015	0.0062	0.0004
Cs	0.019	0.003	0.019	0.003	0.014	0.006	0.010	0.002	-	-	0.023	0.017	0.001	0.001
Ba	0.0364	0.0087	0.0373	0.0152	0.0388	0.0261	0.0288	0.0091	-	-	-	-	0.00004	0.00004
La	4.787	0.646	2.591	0.240	4.658	0.962	3.049	0.132	0.410	0.037	0.542	0.043	0.769	0.071
Ce	7.199	0.756	6.229	0.646	5.199	1.073	3.190	0.129	0.377	0.028	0.547	0.061	1.591	0.120
Nd	16.105	1.537	28.430	4.210	6.454	1.630	3.759	0.147	0.579	0.054	0.925	0.114	2.632	0.155
Sm	17.843	1.414	47.245	7.699	5.215	1.293	3.113	0.137	0.388	0.070	0.767	0.182	3.522	0.421
Eu	16.403	1.341	53.195	8.181	4.743	1.132	2.900	0.133	0.275	0.082	0.682	0.192	3.372	0.196
Dy	9.027	0.537	27.082	3.925	2.619	0.460	1.521	0.073	0.329	0.057	0.388	0.088	2.798	0.220
Tm	4.773	0.261	9.067	0.903	2.937	0.279	1.567	0.097	1.330	0.145	2.860	0.890	1.846	0.182
Yb	4.797	0.249	7.015	0.600	3.937	0.296	2.281	0.152	2.564	0.346	8.004	3.116	1.978	0.186
Hf	2.385	0.162	3.556	0.472	1.802	0.118	1.141	0.123	2.443	0.275	3.702	0.479	0.769	0.065
Ta	0.496	0.152	2.3694	0.6244	0.6502	0.2545	1.5654	0.2337	2.1082	0.1764	3.6854	0.6561	0.0153	0.0013
Pb	0.079	0.017	0.0587	0.0152	0.1142	0.0349	0.0199	0.0130	0.0884	0.0280	0.0564	0.0536	0.0203	0.0040
Th	0.201	0.034	0.3565	0.0419	0.3172	0.0321	0.2892	0.0239	0.0798	0.0240	0.0709	0.0276	0.0040	0.0003
U	-	-	0.0512	0.0331	0.1261	0.0272	0.0196	0.0103	0.0460	0.0245	0.0834	0.0342	0.0022	0.0003

Table 5: Coefficients for prediction of lattice-strain parameters for clinopyroxene ${}^{VI}M1$ and ${}^{VIII}M2$ sites from clinopyroxene composition, temperature and pressure. Fitted vs. predicted lattice-strain parameters and partition coefficients are in Figures 12–13 and full multiple linear regression reports are available in Appendix E.

Model for $\ln D_0, {}^{VIII}M2$ site (n = 82)			Model for $\ln D_0, {}^{VI}M1$ site (n = 16)		
Parameter	Coefficient	σ	Parameter	Coefficient	σ
Intercept	4.52	0.91	Intercept	5	1
${}^{VI}M1Ti$	6.8	3	TAl	4	0.5
${}^{VI}M1Al - {}^{VI}M1Fe^{3+}$	1.6	0.6	${}^{VI}M1Fe^{2+}$	2.6	0.9
${}^{VIII}M2Fe^{2+}$	-3.8	1.3	${}^{VIII}M2Na$	-8	1
T [K]	-0.0035	0.0007	${}^{VIII}M2Ca$	-3	2
TAl + TFe $^{3+}$	2.6	0.8			
R^2		0.647			0.959

Model for $E_s, {}^{VIII}M2$ site (n = 79)			Model for $E_s, {}^{VI}M1$ site (n = 18)		
Parameter	Coefficient	σ	Parameter	Coefficient	σ
Intercept	247	44	Intercept	-2322	298
${}^{VI}M1Al$	-424	144	T [K]	3.2	0.4
${}^{VI}M1Mg$	-285	102	P [GPa]	-408	145
${}^{VI}M1Ti$	-1145	378	${}^{VI}M1Mg$	-800	212
${}^{VIII}M2Mg$	-306	115			
P [GPa]	37	12			
TAl + TFe $^{3+}$	313	102			
XMg	336	102			
R^2		0.348			0.936

Model for $r_0, {}^{VIII}M2$ site (n = 82)			Model for $r_0, {}^{VI}M1$ site (n = 16)		
Parameter	Coefficient	σ	Parameter	Coefficient	σ
Intercept	1.01	0.02	Intercept	0.79	0.03
${}^{VI}M1Ti$	0.16	0.05	P [GPa]	-0.017	0.005
${}^{VI}M1Al - {}^{VI}M1Fe^{3+}$	-0.03	0.01	${}^{VIII}M2Mg$	-0.48	0.06
${}^{VIII}M2Ca$	0.09	0.02	${}^{VI}M1Fe^{3+}$	0.14	0.03
${}^{VIII}M2Na$	0.14	0.02	${}^{VIII}M2Ca$	-0.05	0.02
T [K]	-4.46E-05	1.22E-05			
R^2		0.846			0.987

1687 7. Supplementary figures

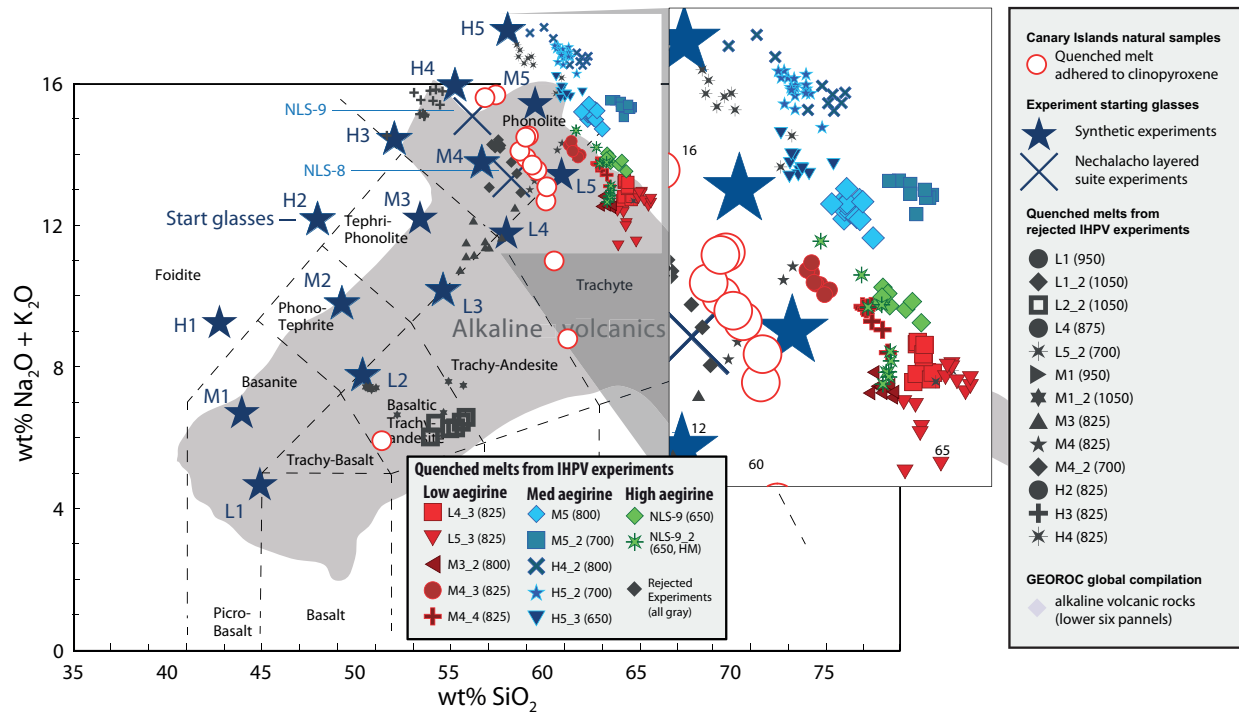


Figure S1: Total alkalies vs. silica diagram for glasses produced in internally heated pressure vessel experiments and adhered to Canary Islands clinopyroxene phenocrysts (Le Bas et al., 1986). Large stars indicate synthetic starting glass compositions as used in internally heated pressure vessel experiments (Table 1), whereas large crosses indicate the composition of powdered natural samples from the Nechalacho layered suite, NT, Canada that were used as starting materials for some experiments. The gray field indicates the compositional range expressed by alkaline volcanic provinces from around the world, sourced from the GEOROC database. Rejected experiments in dark gray are not discussed in the main text, and either did not produce clinopyroxene, produced crystals that were too small for analysis by LA-ICP-MS, or grew crystals during quench, hence preserving disequilibrium partitioning behaviour. Further diagrams showing major-element compositions for the quenched melts and the starting glasses are in Fig S2.

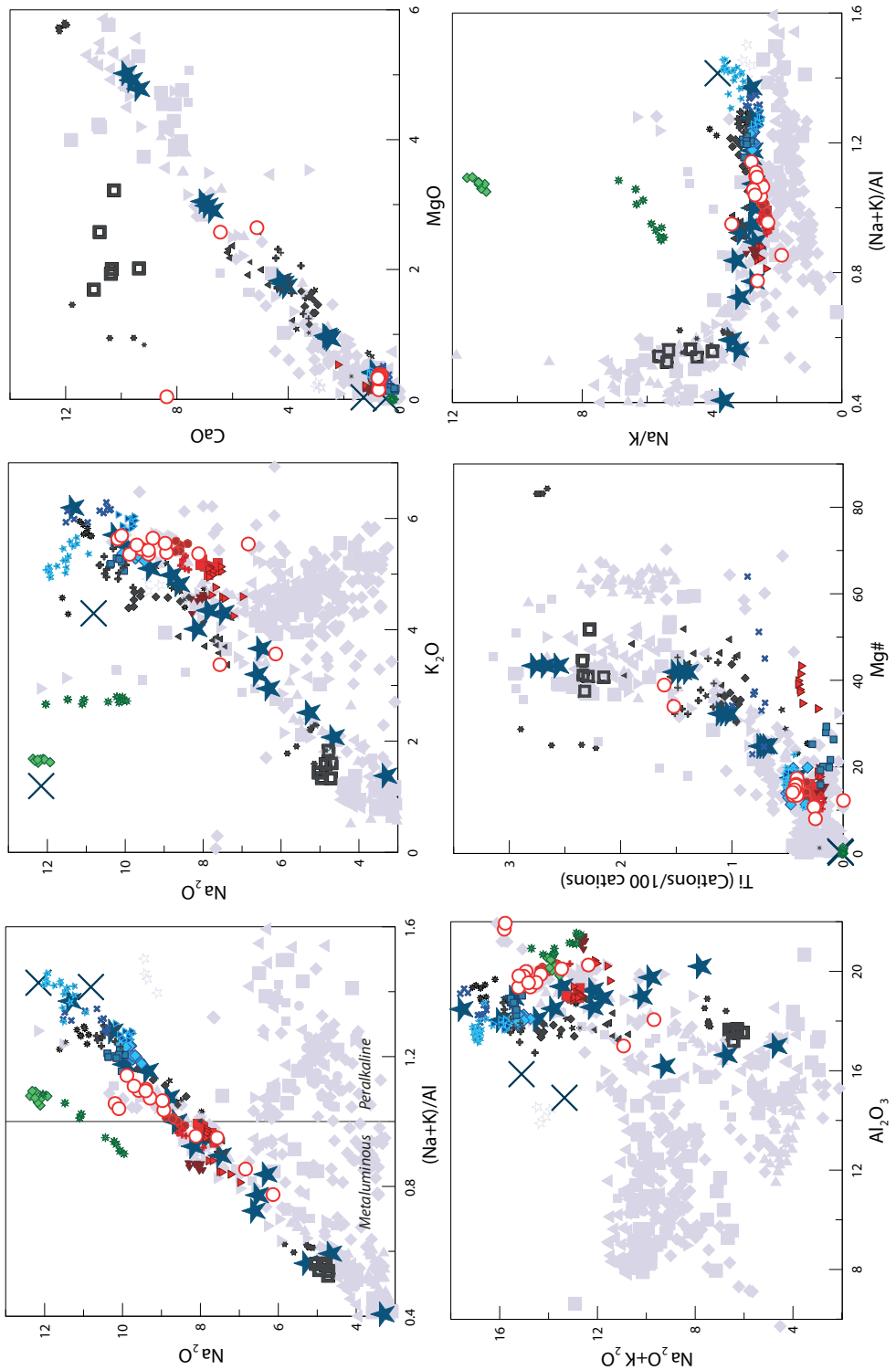


Figure S2: Major-element compositions for glass produced in the internally heated pressure vessel experiments and adhered to clinopyroxene phenocrysts from the Canary Islands. Symbols as in Fig. S1.

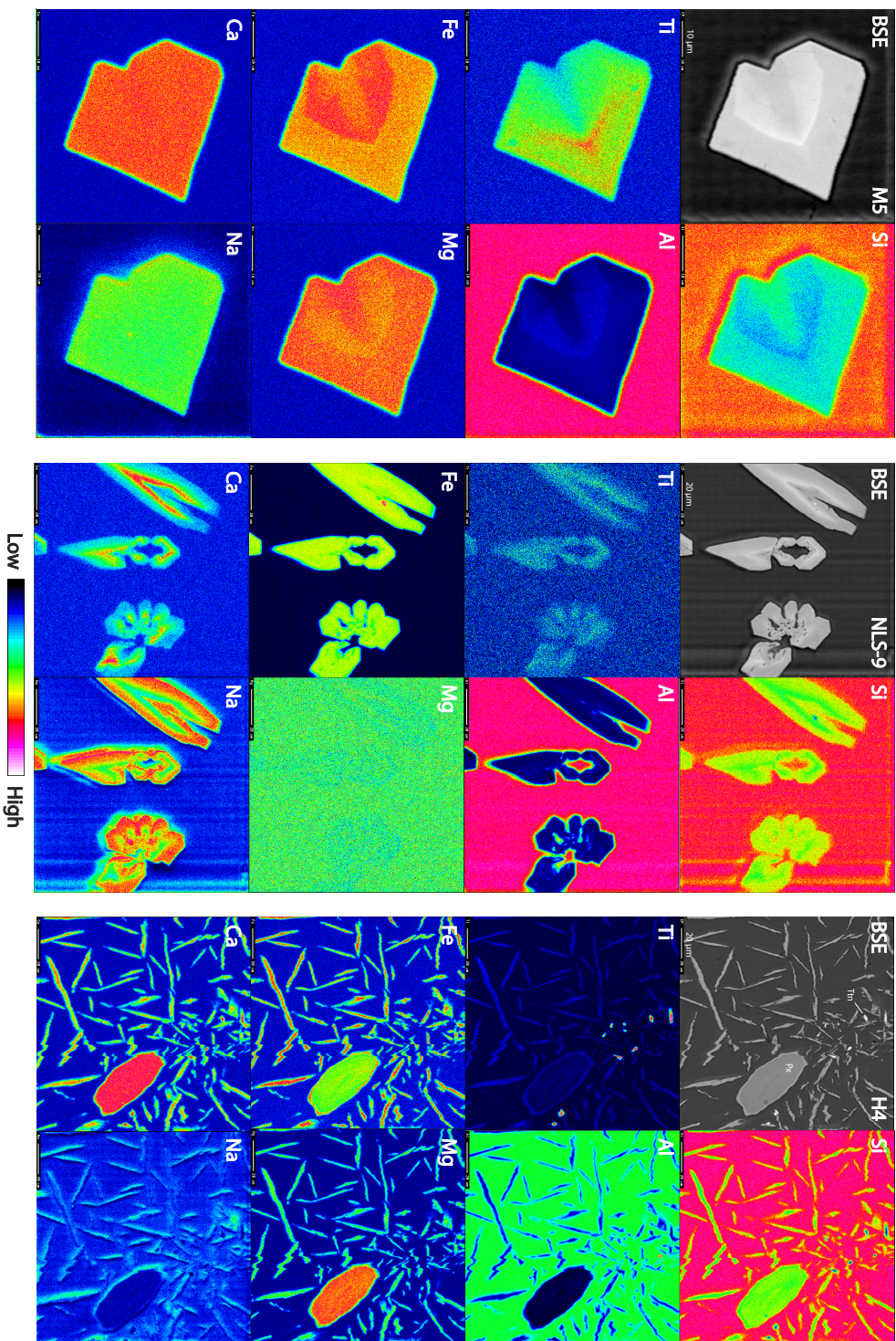


Figure S3: Element maps of clinopyroxene from internally heated pressure vessel experiments. M5 clinopyroxene have a sharp internal boundary that reflects feldspar saturation and are subtly zoned. NLS-9 clinopyroxene are more strongly zoned with swallowtail and hopper textures and rare inclusions of magnetite (cf. Walker et al., 1976; Lofgren, 1989; Shea and Haenner, 2013). H4 clinopyroxene (Px) display a bimodal crystal size distribution and occur with titanite (Tm). The bimodal crystal size distribution is due to a temperature perturbation during run, and renders this experiment unsuitable for this element-partitioning study.

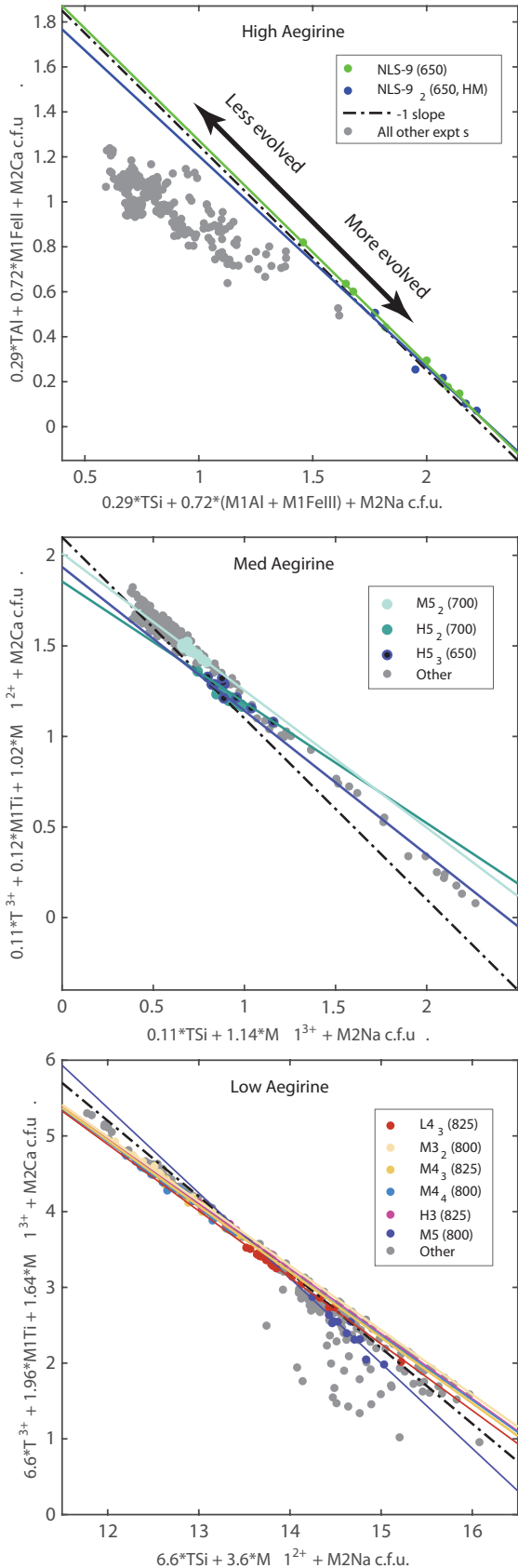


Figure S4: Major-element exchange mechanisms for (a) high, (b) medium and (c) low-aegirine clinopyroxene generated in internally heated pressure vessel experiments. Each individual plotted point represents an electron-microprobe analysis. Iron in the clinopyroxene was assigned to 2+ or 3+ valence following Droop (1987), then major-element cations were assigned to sites following Morimoto (1989, see Appendix F). Axes were defined by linear regressions between site-assigned major-element abundances, which have been checked for consistency in total site-occupancy and for charge.

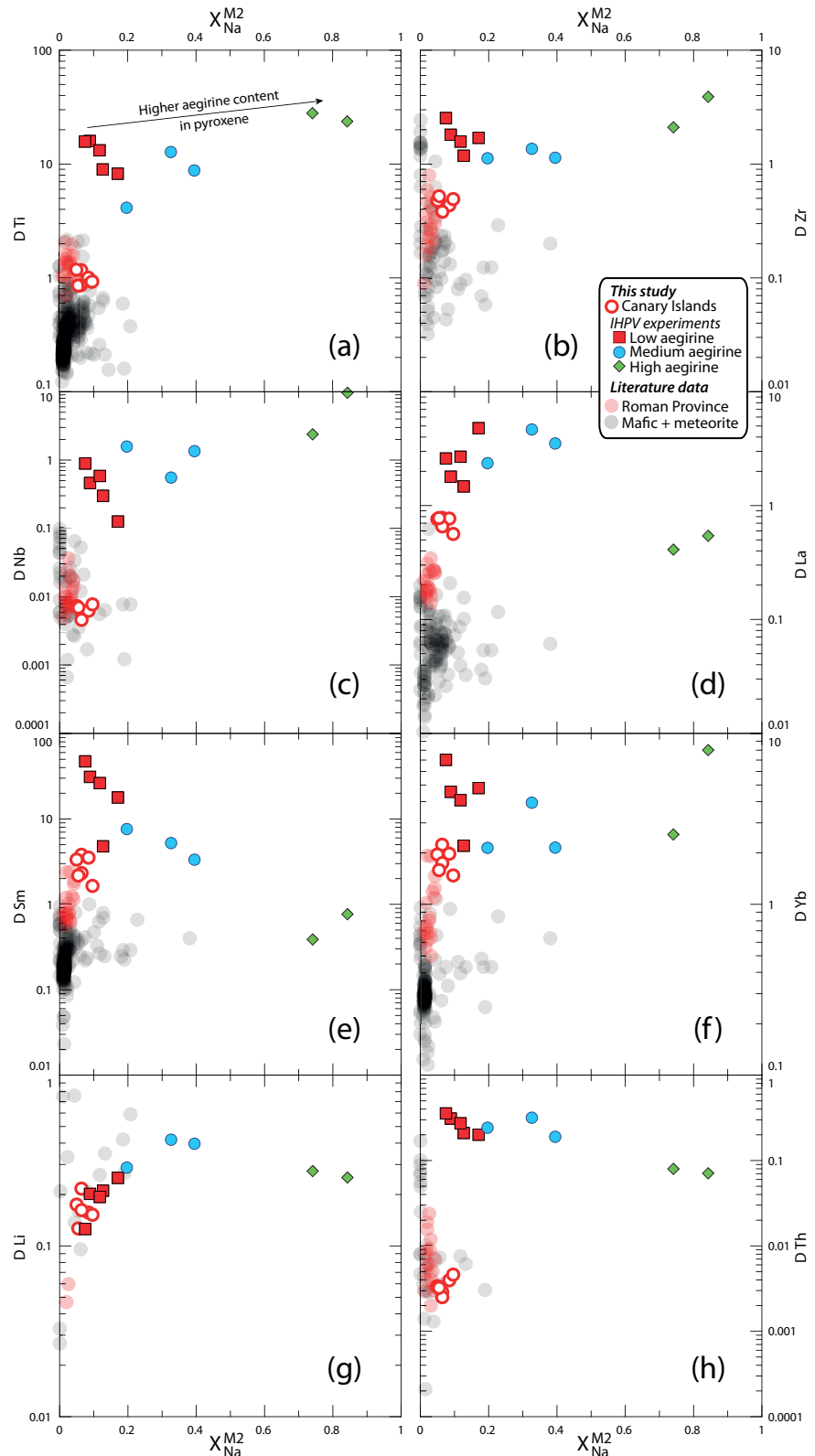


Figure S5: Element partitioning coefficients for HFSE (Ti, Zr, Nb), REE (La, Sm, Yb) and TE (Li, Th) vs. $X_{\text{Na}}^{\text{M2}}$. Literature values ($n = 411$), including those from Italian volcanoes, are from the compilation of Bédard (2014).

1688 **Appendix A. Electronic appendix of chemical data (.xlsx)**

1689 Electronic appendix (.xlsx file) containing experiment starting glass compositions, experiment run conditions, mineral
 1690 abundances in experimental charges, compositions of reference materials used for EPMA and LA-ICP analyses,
 1691 major-element concentrations for experiment glasses and clinopyroxene, partition coefficients and fitted lattice-strain
 1692 parameters.

1693 **Appendix B. Locations for the Canary Islands samples (.kml)**

1694 Electronic appendix (.kml file) containing field locations for the Canary Islands samples.

1695 **Appendix C. The Laser Ablation ICP-MS unmixing model**

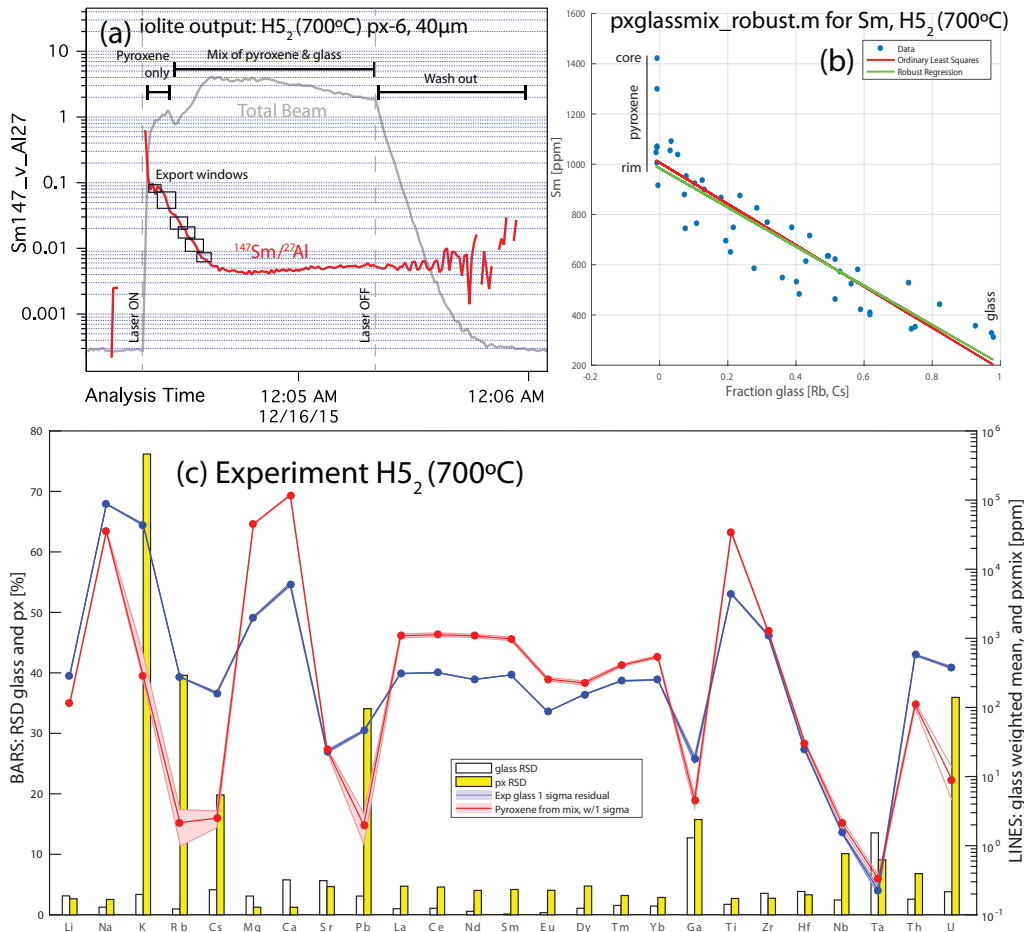


Figure C.6: An example of the robust regression data reduction scheme for laser-ablation ICP-MS analyses of glass and clinopyroxene mixtures. (a) Time series of laser-ablation data as displayed in by the iolite v2.5 extension for Igor Pro (Paton et al., 2011), (b) a MATLAB output diagram from the robust regression unmixing script, and (c) a quality control diagram output from the same MATLAB script.

1696 The LA-ICP-MS robust regression data reduction scheme described here allows for determination of mineral trace-
 1697 element compositions where the grains of interest are smaller than the laser spot-size. The mathematics underpinning

1698 the script are similar those of Rubatto and Hermann (2007) and from our research group, of Yang et al. (2018).
1699 Assumptions include...

1700 whilst effectively rejecting outlier data, for example from the ablation of minerals other than clinopyroxene that
1701 may have been hidden below the polished surfaces of the grain mounts

1702 Initially, the raw counts-per-second data are imported into Igor Pro, running the iolite v2.5 extension (Paton et al.,
1703 2011) where drift and background corrections are made. Mixed signals of clinopyroxene show characteristic stepped
1704 peaks in element-ratio and beam intensity traces (Figure C.6a). Outputs are exported in short time windows as shown.

1705 Trace-element concentrations in the mixes are then normalised to the sum of major-element oxides, as measured by
1706 LA-ICP-MS.

1707 TO COMPLETE

1708 (a) Time series of laser-ablation data, showing traces for Sm/Al (red) and total beam intensity (gray). The laser
1709 beam often ablated through the small clinopyroxene crystals, returning a mixed signal that was exported from the
1710 iolite data reduction software in short time windows as shown. Data were then normalised to the sum of major-
1711 element concentrations and mixes were deconvolved using a robust regression script written in MATLAB. (b) An
1712 example output diagram for the robust regression data reduction scheme. Clinopyroxene–glass mixing ratios were
1713 constrained by strongly incompatible elements Rb and Cs. For each element, a robust linear regression was defined
1714 between the fraction of glass in the mixture and element concentration. The intercept of this regression with zero glass
1715 returned the trace-element concentrations in the clinopyroxene. Uncertainty with this technique is typically below 10
1716 % relative (median 9.3 % at the 1σ level). In this example, the Sm-rich core of a zoned clinopyroxene crystal is
1717 effectively rejected during data processing, and the derived Sm concentration for the clinopyroxene is therefore closer
1718 to that of the clinopyroxene rims that are in equilibrium with the adjacent quenched melt. (c) A quality control
1719 diagram output from the MATLAB data reduction scheme showing the concentrations of various elements in the
1720 glass and clinopyroxene (lines) and the uncertainty on these concentrations expressed as a relative standard deviation
1721 (bars). Derived partition coefficients (D_i) are the mass concentration of element ‘ i ’ in clinopyroxene divided by that
1722 in the adjacent quenched melt. Residuals for the D_i values were calculated using uncertainties derived from the
1723 clinopyroxene and glass analyses to calculate minimum and maximum partition coefficients at the 1σ level. These are
1724 reported in Table 4 and Appendix A

1725 **Appendix D. EPMA Ce concentration transects across experiment clinopyroxene (.xlsx)**

1726 Electronic appendix (.xlsx file) containing electron-microprobe transects across experiment clinopyroxene for Ce,
1727 Mg and Fe. The data indicate that $D_{Ce}^{px/melt}$ values determined from our experiments are overestimates, but only by up
1728 to 25%. Sector zoning in the clinopyroxene appears to have a larger impact on apparent Ce partitioning behaviour
1729 than growth zoning.

1730 **Appendix E. Multiple linear regression reports (.pdf)**

1731 Electronic appendix (.pdf file) containing multiple linear regression reports from the stepwise fitting of 3+ cation
1732 lattice-strain parameters for the predictive model for element-partitioning (39 pages).

1733 **Appendix F. Numerical model for prediction of clinopyroxene/melt element-partitioning coefficients for ions of
1734 3+ valence (.xlsx)**

1735 Electronic appendix (.xlsx file) containing a numerical model for prediction of clinopyroxene/melt element-
1736 partitioning coefficients for ions of 3+ valence. Required input data are major-element oxide compositions for
1737 clinopyroxene, pressure and temperature. The model for the $VIII$ M2 site is calibrated for application to systems of
1738 basaltic to peralkaline phonolite composition. The model for the VI M1 site is calibrated for use on alkaline to weakly
1739 peralkaline systems where the aegirine mol% in clinopyroxene does not exceed 50.

1740 **Appendix G. Supplement: Chemical heterogeneity and the approach to equilibrium during the experiments**

1741 *Appendix G.1. Attainment of equilibrium in the Canary Islands rocks*

1742 The Canary Islands trace-element partition-coefficients presented here were determined from euhedral, blade-
1743 shaped crystals free of melt inclusions and chemical zonation. The corresponding quenched melt was in direct contact
1744 with these crystals and shows no zonation in backscattered electron images (Fig. 1). While equilibrium conditions
1745 are challenging to confirm for a natural volcanic system, the euhedral forms, chemical homogeneity of crystals, and
1746 congruency between samples from separate eruptions suggest that the crystals grew in a stable environment, and were
1747 not subject to chemical or physical perturbations during growth (Fig. 6).

1748 *Appendix G.2. Attainment of equilibrium in the experiments*

1749 Experiments used to determine trace-element partition-coefficients must have attained, or at least closely ap-
1750 proached, chemical equilibrium. Unfortunately no experiments are able to determine equilibrium trace-element
1751 partition-coefficients *sensu stricto* because reversal experiments, where a clinopyroxene re-equilibrates with a melt,
1752 are not possible owing to sluggish diffusion of most elements through the clinopyroxene structure (Van Orman et al.,
1753 2001; Zhang et al., 2010). The following two sections discuss some analytical and experimental biases that must be
1754 considered when determining mineral-melt trace-element partition-coefficients from crystallisation experiments.

1755 *Appendix G.2.1. The formation of diffusive boundary layers*

1756 A potential barrier to chemical equilibration during crystallisation is the formation of a diffusive boundary layer
1757 within the melt adjacent to growing crystals. In a perfect equilibrium case there are no compositional gradients in
1758 the melt at any time during crystal growth. However in reality the growth of crystals depletes compatible elements
1759 from the melt and residually enriches incompatible elements. Theoretically, this process of crystal growth results
1760 in formation of a (potentially ephemeral) diffusive boundary layer in the melt directly adjacent to the crystal that is
1761 depleted with respect to compatible elements and enriched with respect to those that are incompatible (Lu et al., 1995).
1762 The composition of such a diffusive boundary layer depends on both the relative enrichment or depletion of elements
1763 during the crystallisation process, and the rate at which these elements diffuse through the melt. Rapidly-diffusing
1764 elements with partition-coefficients close to unity will have concentrations closest to that of the bulk melt.

1765 Experiments designed to investigate trace-element-partitioning behaviour might employ slow cooling rates to limit
1766 the development of diffusive boundary layers, thus forming crystals from melt that is closer in composition to that of
1767 the bulk experiment. Such experiments then run into another problem, in that significant crystallisation may occur at
1768 temperatures above that of the final run temperature. Rapidly-cooled experiments circumnavigate this issue, but may
1769 form relatively more pronounced diffusive boundary layers during crystal growth that become ‘flattened out’ during
1770 the homogenisation stage of the experiment.

1771 Numerous diffusion data have been gathered for silicate melts over the past few decades, and a comprehensive
1772 review is given by Zhang et al. (2010). Diffusion of trace-elements through water-saturated peralkaline melts is rapid,
1773 owing to their depolymerised structure. For example Lanthanum diffusion-coefficients are 6 orders of magnitude
1774 higher than for water-saturated granitic compositions of a similar temperature (compare Rapp and Watson, 1986;
1775 Behrens and Hahn, 2009). This rapid diffusion serves to minimise the formation of diffusive boundary layers adjacent
1776 to growing crystals in our experiments. Coupled diffusion mechanisms complicate the application of measured single-
1777 element diffusion-coefficients to a crystallising system (Grove et al., 1984; Liang et al., 1994; Costa et al., 2003). Here,
1778 the diffusive flux of trace-elements may be coupled to gradients in major-element concentration within the melt.

1779 To investigate the impact of diffusive effects on trace-element-partitioning between clinopyroxene and melt, Mollo
1780 et al. (2013) performed crystallisation experiments on trachybasaltic melts at a range of cooling rates (2.5–50°C /
1781 hr). Rapid cooling rates result in depletions of Si, Ca and Mg in the clinopyroxene that are compensated for by
1782 enrichments in Al, Na and Ti. Regardless of cooling rate, Ounma parabolae could be fitted through isovalent sets
1783 of partition-coefficients, indicating that crystal-lattice-effects dominated over those associated with the formation of
1784 diffusive boundary layers and that local equilibrium was achieved at the time of crystallisation. In their rapidly-cooled
1785 experiments Mollo et al. (2013) found apparent clinopyroxene/melt trace-element partition-coefficients that varied
1786 with identical crystal-chemical systematics to true equilibrium partition coefficients, the magnitude of both sets of
1787 trace-element partition-coefficients following the ^{IV}Al content of the clinopyroxene (*ibid.*, their Fig. 9). Deviations of

1788 the partition coefficient of several orders of magnitude can be obtained only when rapidly growing crystals entrap small
1789 portions of the diffusive boundary layer that are found as minute melt inclusions randomly distributed in the mineral
1790 phase (Kennedy et al., 1993). In this extreme case, partitioning behaviour is obviously influenced by contamination
1791 phenomena and no Onuma parabolae can be derived. As Onuma parabolae could successfully be fitted through
1792 partitioning data for all of our presented experiments (see following sections), and no melt inclusions were observed
1793 in optical and electron imaging, we infer that our data were not affected by the presence of such melt inclusions, and
1794 that they may be compared directly with partitioning data derived from experiments that employed slower cooling
1795 rates.

1796 *Appendix G.2.2. Chemical zonation in the experiment clinopyroxene: Theoretical framework*

1797 Trace-elements diffuse slowly through the clinopyroxene structure relative to that of the melt (Van Orman et al.,
1798 2001; Zhang et al., 2010), therefore no re-equilibration of trace-elements takes place on an experimental time scale.
1799 Strictly speaking, clinopyroxene only record true equilibrium conditions at their outermost rim. Experiments designed
1800 for the derivation of equilibrium partition coefficients ideally minimise bias by limiting the fraction of crystallisation,
1801 producing minerals that are as homogeneous as possible. Currently available *in situ* analytical techniques for trace-
1802 element abundances, such as LA-ICP-MS and SIMS, are limited in terms of minimum beam-size to $\sim 10 \mu\text{m}$; chemical
1803 zonation, however subtle, will be continuous from the core to the rim of the mineral. Consequently, no experimentally-
1804 derived partition-coefficients record chemical equilibrium *sensu stricto*, but properly conducted experiments may
1805 closely approximate this state.

1806 Because only the very rim of a crystal records chemical equilibrium with the adjacent melt, and some internal por-
1807 tions of the minerals must be sampled during *in-situ* analyses all experimentally-determined trace-element partition-
1808 coefficients are biased toward higher values for compatible elements and lower values for incompatible elements. The
1809 magnitude of these biases depends on the fraction of crystallisation in the experiment, the true equilibrium partition-
1810 coefficient of that element, as well as the proportion of each growth-zone sampled during the *in-situ* analysis. Fortu-
1811 nately *in-situ* chemical analyses preferentially sample the mantle and rim of zoned crystals because few analyses
1812 section a crystal perfectly through the core. As a result there is a sampling bias toward equilibrium mineral composi-
1813 tions.

1814 Consider a hypothetical experimental system in which 20% of the melt crystallises as a single mineral, and where
1815 the chemical analyses of that mineral are truly bulk averages of that mineral composition. An incompatible element
1816 with a true equilibrium partition coefficient of 0.1 would return a measured partition coefficient of 0.09, a small
1817 bias because the concentration of that incompatible element in the melt changed only subtly during the course of
1818 crystallisation. For compatible elements with true D_i values of ~ 10 , measured partition coefficients can be a factor of
1819 2–3 higher than true partition coefficients, because their concentration in the melt changes more than an incompatible
1820 element during the course of crystallisation.

1821 Further complexity is introduced in systems that crystallise multiple minerals simultaneously. In the case of ex-
1822 periment M3₂, the REE are compatible in clinopyroxene, but are incompatible in biotite and oxides (e.g. Mahood
1823 and Stimac, 1990; Schmidt et al., 1999). The REE have therefore been residually enriched in the melt phase by the
1824 crystallisation of biotite and oxide minerals, while simultaneously being depleted from the melt by crystallisation of
1825 clinopyroxene. These two competing processes serve to minimise the effect of fractional crystallisation on the
1826 concentration of trace-elements in the melt and consequently derived REE partition-coefficients between clinopyroxene
1827 and melt will be closer to true equilibrium values.

1828 *Appendix G.2.3. Implications of the cerium zonation across the experiment clinopyroxene*

1829 Electron-microprobe analyses offer a smaller minimum beam-size than LA-ICP-MS systems at the expense of
1830 precision and of number of elements that may be analysed simultaneously. This higher spatial resolution permitted
1831 investigation of the zonation of Ce concentrations within the experiment clinopyroxene, with Ce as a proxy for the
1832 other compatible elements.

1833 The magnitude of concentric growth zoning in the experiment clinopyroxene was examined by averaging bulk and
1834 rim compositions across multiple sector-zoned grains within each experiment. The median Ce counts divided by the
1835 rim Ce counts was 1.04 for experiment M3₂, 1.08 for experiment M5 and 1.12 for the fluorine-bearing experiment
1836 M3-1.25F (see Beard, 2018). Contrary to theory discussed above, the subtly (3%) crystallised experiment M5 shows
1837 a greater variation in core-to-rim Ce content than the more heavily (?? TO ADD%) crystallised experiment M3₂.

1838 Furthermore, the $D_{Ce}^{cpx/melt}$ for experiment M3₂ (6.2) is approximately double that for experiment M5 (see discussion
1839 below), which should further promote the formation of Cerium zonation in the clinopyroxene during crystallisation.
1840 Consequently it is possible that many existing experimentally-derived trace-element partition-coefficients are system-
1841 atically offset from true equilibrium values.

1842 If Cerium is used as a proxy for the behaviour of compatible elements in our experimental system, then apparent
1843 partition coefficients derived for these elements via LA-ICP-MS are systematically offset to higher values by 4–
1844 8%. Such a systematic bias is small, relative to the variation in clinopyroxene-melt partition coefficients within our
1845 sample set, as well as in the literature. The effect of crystal zonation on incompatible element concentrations was not
1846 measured, but as outlined in the theoretical framework above, this effect should be smaller than that for the compatible
1847 elements. No correction factor has been applied to the data presented in the figures below, or in Table 4 and Appendix
1848 A.